Electronic Supplementary Material (ESI) for Journal of Materials Chemistry A.

Supplementary Information

Arylboron Functional Covalent Organic Frameworks for Synergistic Photocatalytic Hydrogen Evolution

Xuan Wu[a], Mingcai Zhang[a], Yusong Xia[a], Chenglong Ru[a], Peiyan Chen[a], Hao Zhao*, [a, b], Lian Zhou[c], Chenliang Gong*, [a], Jincai Wu[a], Xiaobo Pan*, [a, c]

[a]State Key Laboratory of Applied Organic Chemistry (Lanzhou University), Key Laboratory of Nonferrous Metal Chemistry and Resources Utilization of Gansu Province, College of Chemistry and Chemical Engineering, Lanzhou University, Lanzhou 730000, People's Republic of China.

[b]School of physics and electronic information, Yantai University, 30 Qingquan Road, Yantai 264005, China.

[c]New Energy (Photovoltaic) Industry Research Center, Qinghai University, Xining 810006, China.

1. Materials

Phloroglucin, 1,3,5-triformylbenzene (**TFB**), trifluoroacetic acid (**TFA**), 4-bromo-2,6-dimethylaniline, boron trifluoride ethyl etherate (**$BF_3·Et_2O$**), N, N'-dimethylenediamine (**DMEDA**), tert-butyl carbamate (**NH_2Boc**) and copper iodide (**CuI**) were purchased from Energy Chemical. Triethylamine (**TEA**), triethanolamine (**TEOA**), ascorbic acid (**AA**) and hexachloroplatinic acid were purchased from Macklin. Tetrahydrofuran (**THF**) and diethyl ether (**Et_2O**) were purchased from commercial sources and dried with sodium through a Schlenk line. The water used in the experiment is distilled water (pH = 6.08, σ = 2.12 μS/ cm, T = 20.0 °C). Unless additional mentioned, other reagents were purchased from commercial sources and used without further purification.

2. Instrumentation

2.1 Fourier Transform Infrared (FT-IR) spectroscopy

FT-IR spectroscopy measurements were recorded in a Perkin Elmer Spectrum 100 with a PIKE Technologies MIRacle Single Reflection Horizontal ATR Accesory with a spectral range of 4000-400 cm^{-1} using the KBr disk method.

2.2 Powder X-ray diffraction (PXRD)

PXRD patterns were measured on a MiniFlex600 (Rigaku) Bragg-Brentano geometry with a Cu-$K\alpha_1$-radiation (λ =1.540593 Å). Samples were mounted on a flat sample plate. Patterns were collected in the $3.01° < 2\theta < 40°$ range with a step size of 0.02° and scan speed of $10°·min^{-1}$.

2.3 Thermogravimetric analyses (TGA)

TGA analysis of samples was run on a Thermobalance NETZSCH STA 449F3 thermal gravimetric analyzer with samples held in an aluminum oxide pan under nitrogen flow (60 mL/min). A 10 $K·min^{-1}$ ramp rate was used from 35 to 800 ^oC.

2.4 Solution nuclear magnetic resonance (NMR) spectroscopy

^1H and ^{13}C NMR spectra were recorded in solution using a JEOL JNM-ECS-400 with a 5 mm FG/RO Digital Auto Tune Switchable Probe at room temperature in ppm downfield from TMS.

2.5 Solid-state cross-polarization magic-angle spinning (CP-MAS) NMR spectroscopy

The Solid-state ^{13}C and ^{11}B CP-MAS NMR spectra were recorded on an Agilent 600 DD2 spectrometer (Agilent, USA, magnetic field strength 14.1 T). The powder samples were placed in a pencil-type zirconia rotor of 4.0 mm o.d.

2.6 Optical diffuse reflectance spectra

UV-visible absorption spectra of the materials were collected at room temperature with a UV-Vis NIR diffuse reflectance spectrometer Perkin Elmer Lambda 950+Refle at a photometric range of 300-800 nm. Powders were prepared in a sample carrier with a quartz glass window at the edge of the integrating sphere with $BaSO_4$ as the optical standard. Kubelka-Munk spectra were calculated from the reflectance data.[1, 2]

2.7 Photoluminescence (PL) spectroscopy

PL spectroscopy was collected with a photoluminescence spectrophotometer FL3-21 (Horiba) at room temperature. The time-resolved fluorescence decay spectrum were obtained on a FLS920 spectrofluorometer (Edinburgh Instruments) with an excitation wavelength of 360 nm and detection wavelengths of **TAB-TFB-COF** and **TAB-TFP-COF** are 558 nm and 619 nm, respectively. The average photoluminescence lifetime was estimated using Equation as follows[3]:

$$\tau = \tau_1 R_1 + \tau_2 R_2 + \tau_3 R_3$$

Where τ is average decay time, τ_1, τ_2 and τ_3 are decay times were fitted by triexponenital kinetics function, and R_1, R_2 and R_3 are relative magnitudes.

2.8 X-ray photoelectron spectroscopy (XPS)

The samples were pressed onto indium foil and the spectra were collected on an ESCALAB XI+ (Thermo Fisher Scientific) X-ray photoelectron spectrometer with charge neutralization. All of the XPS spectra presented in the main paper, and all subsequent data analysis were processed using the software XPS Peak Fit 4.1 and performed following subtraction of a Shirley background from the region of interest. The XPS spectra were fitted using components with Gaussian/Lorentzian lineshapes and with full-width-half-maximum (FWHM) values constrained within the range 0.8 ~ 1.6 eV. Neither the energy nor the relative area of the components was constrained. The spectra were referenced to the adventitious C1s peak at 284.800 eV.

2.9 Field-Emission Scanning Electron Microscopy (FESEM)

Scanning electron microscopy studies were performed on a Hitachi S-4800 microscope operating at an accelerating voltage of 5.0 kV. Samples were previously coated with gold in a sputter Quorum Q150T-S.

2.10 Nitrogen adsorption-desorption isotherm measurements

The measurements were measured using a BSD-PS1/2 (Beishide instrument-S&T, Beijing, CO., Ltd.) volumetric instrument with extra-high pure gases. Before the gas adsorption measurements, the as-prepared samples (60.0 mg) were dried under dynamic vacuum at 120 ^{o}C for 10 h. The Brunauer-Emmet-Teller (BET) was carried out to determine the total specific surface areas for the N_2 isotherms at 77 K.

By using the non-local density functional theory (NLDFT) model, the pore size distributions were derived from the sorption curves.

2.11 Photoelectrochemical measurements

The transient photocurrent (TPC) response profiles was recorded via a CHI 760C electrochemical workstation with a standard three-electrode system with the photocatalyst-coated fluoride-tin oxide (FTO) as the working electrode, Pt plate as the counter electrode, and an Ag/AgCl electrode as a reference electrode. 0.2 M Na_2SO_4 solution was used as the electrolyte. The samples (3.0 mg) were added into 2 mL ethanol and 50 μL Nafion mixed solution, and the working electrodes were prepared by dropping the suspension onto FTO glass substrate electrode surfaces and dried at

120 ^{o}C in vacuum oven for 8 h. A 300 W Xenon lamp (CEL-HXF300-T3, Au-light) with a 420 nm cut off filter was used as the light source during the measurement. Under the exposure of visible light irradiation, light-induced transient current responses were recorded at five periodic on-off cycles. The electrochemical impedance spectroscopy (EIS) was performed in the frequency range from 10^{-1} to 10^{5} Hz with a bias potential of +1.5 V. The Mott-Schottky plots were obtained with a bias potential that ranged from -0.5 to 0.5 V (vs Ag/AgCl) under the frequency of 800, 1000, and 1500 Hz, respectively.

2.12 Zeta potential measurements

All measurements were carried out on a Zetasizer Nano ZS analyzer (90Plus Pals, Brookhaven Instruments, U.S.). The measurements were performed at 25 °C and were repeated three times to gain an average value.

2.13 Electron paramagnetic resonance (EPR) measurements

All EPR spectra were recorded on the electron paramagnetic resonance spectrometer (ER200DSRC10/12, Bruker, Germany) at room temperature under the ambient atmosphere. Traditionally, 3 mg photocatalyst was transferred to a foil wrapped NMR tube, and overnight in dark. The EPR spectra were recorded before and after a 5 min radiation with a 300 W Xenon lamp (CEL-HXF300-T3, Au-light) euqipped with a 420 nm cut off filter.

2.14 Photocatalytic activity measurements

Traditionally, a custom glass light reactor with 12.5 mg photocatalyst power was added in 25 mL aqueous solution (V_{H_2O}:V_{MeOH} = 4:1) containing ascorbic acid (0.44 g, 0.1M) as sacrificial electron donor. The reaction temperature is kept at 20 °C and Pt was loaded on the surface of catalyst by in situ photo-reduction H_2PtCl_6 (6.5 μL, 3% loaded). A 300W xenon lamp (CEL-HXF300-T3, Au-light) fitted with a cut off filter (λ> 420 nm) served as light source. Before photocatalytic reaction, the reactant solution was sonicated at room temperature for 15 min and evacuated with N_2 for 30 min to remove air completely. The generated gas was analyzed on a gas chromatography (Varian, 450-GC, N_2 carrier) equipped with a thermal conductive detector every 1 h. The photocatalytic hydrogen evolution rates were determined from linear regression fit and the pressure increase was neglected in the calculations. All recovered photocatalysts were washed with acetone and dried at 70 °C for further characterization.

2.15 Apparent quantum yields (AQY) measurements

The AQY was measured using the same apparatus as the photocatalytic H_2 evolution test. 12.5 mg **TAB-TFP-COF** was suspended in 25 mL (V_{H_2O}:V_{MeOH} = 4:1) of 0.1 M ascorbic acid solution containing appropriate H_2PtCl_6. The solution was illuminated by 300 W Xe lamp (CEL-HXF300-T3, Au-light) equipped with filter at 420, 450, 500, 550 and 600 nm. The hydrogen evolution of photocatalytic reaction was calculated within 5h. The amount of hydrogen evolution was tested using gas chromatography and the incident photons were measured using a ThorLabs S120C photodiode power sensor. The AQY was estimated using Equation as follows:

$$AQY = \frac{N_e}{N_p} \times 100\%$$

$$= \frac{2 \times M \times N_A}{E_{total}/E_{photon}} \times 100\%$$

$$= \frac{2 \times M \times N_A}{(S \times P \times t)/\left(h \times \frac{c}{\lambda}\right)} \times 100\%$$

$$= \frac{2 \times M \times N_A \times h \times c}{S \times P \times t \times \lambda} \times 100\%$$

Where, M is the amount of H_2 (mol), N_A is Avogadro constant (6.022×10^{23} mol^{-1}), h is the Planck constant (6.626×10^{-34} J s), c is the speed of light (3×10^8 m s^{-1}), S is the irradiation area (cm^2), P is the intensity of irradiation light (W cm^{-2}), t is the photoreaction time (s), λ is the wavelength of the monochromatic light (m).

2.16 Structural simulation

Molecular modeling of all COFs was generated with the Accelrys Materials Studio (ver. 8.0)[4] suite of programs. Pawley refinement was carried out using Reflex, a software package for crystal determination from PXRD pattern. Unit cell dimension was set to the theoretical parameters. The lattice models (cell parameters, atomic positions, and total energy) were fully optimized using Materials Studio Dmol3 molecular dynamics module method. $P1$ space group was chosen for the primitive models in the initial simulations. The Pawley refinement was performed to optimize the lattice parameters iteratively until the R_{wp} value converges and the overlay observed with refined profiles show good agreement. The pseudo–Voigt profile function was used for whole profile fitting and Berrar–Baldinozzi function was used for asymmetry correction during the refinement processes. The final R_{wp} and R_p values were R_{wp} = 11.60 % and R_p = 8.66 % for **TAB-TFB-COF** AA-Stack, R_{wp} = 6.93 % and R_P = 5.45 % for **TAB-TFB-COF** AB-Stack, R_{wp} = 13.57 % and R_P = 9.57 % for **TAB-TFP-COF** AA-Stack and R_{wp} = 9.94 % and R_P = 7.12 % for **TAB-TFP-COF** AB-Stack, respectively.

2.17 Density functional theory (DFT) calculations

All the DFT calculations were carried out using Accelrys Materials Studio (ver. 8.0)[4]. The Generalized Gradient Approximation (GGA) method was employed to describe ion-electron interactions. The exchange and correlation effects were decorated by the Perdew-Burke-Enzerhof (PBE) function with Dmol3 molecular dynamics module method.

3. Synthesis

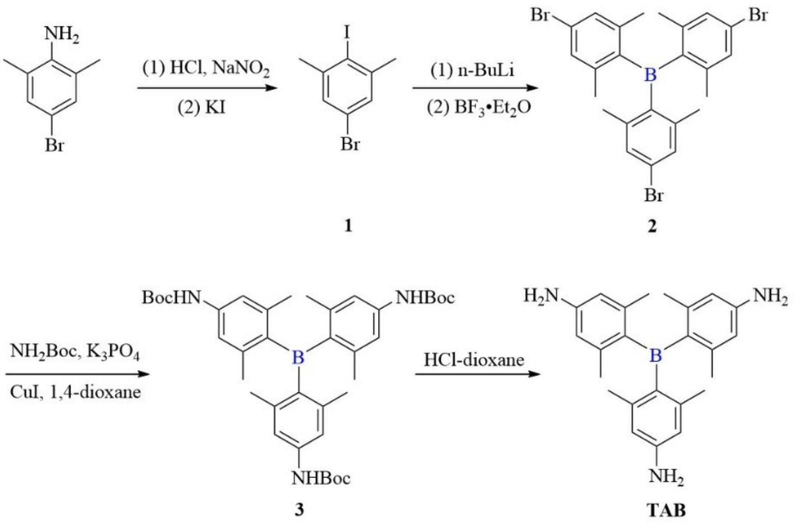

Scheme S1. The synthetic route of 4,4',4''-boranetriyltris(3,5-dimethylaniline) (**TAB**)

4-bromo-2,6-dimethyl iodobenzene (**1**)[5] and tris(4-bromo-2,6-dimethylphenyl)borane (**2**)[6] were synthesized according literatures.

3.1 Synthesis of TAB: In an argon atmosphere, a 100 mL round-bottom with **2** (2.0 g, 3.55 mmol), NH_2Boc (3.33 g, 28.4 mmol), K_3PO_4 (9.04 g, 42.6 mmol), CuI (1.80 g，8.48 mmol) and DMEDA (1.20 mL) were dissolved in 56 mL 1,4-dioxane, the mixture were stirred and refluxed at 100 °C for 48 h. After cooling down to room temperature, the reaction mixture was filtered, and the solid washed with CH_2Cl_2 (100 mL × 2). The organic phase was washed with water (50 mL × 3), dried over anhydrous $MgSO_4$, filtered and the solvent was removed under reduced pressure to get the crude product **3** as a gray solid. Without further purification, the crude product was dissolved in 50 mL chloroform, 20 mL HCl (4 M in 1,4-dioxane) was added and stirred for 12 h. After the reaction, filtered and washed with 50 mL chloroform. The filtered solid was dried in air and dissolved in 100 mL water, the pH was adjusted to 8 by adding $NaHCO_3$, an amount of white solid was precipitated from the solution, extracted with ethyl acetate (100 mL × 3), washed with saturated brine (50 mL), dried with anhydrous $MgSO_4$, filtered, and the solvent was removed under reduced pressure to obtain a pale yellow solid. The residue was further purified by flash column chromatograph using a binary solvent of EA/PE = 1:4 ~ 1:2 as eluent, which allowed the separation of monomer **TAB** as a pale yellow solid (0.92 g, 66 %). ^1H NMR (400 MHz, $CDCl_3$): 6.27 (s, 6H, Ar-H), 3.60 (s, 6H, Ar-NH_2), δ 1.93 (s, 18H, Ar-CH_3). ^{13}C NMR (100 MHz, $CDCl_3$): δ 147.05, 142.73, 114.43, 23.20.

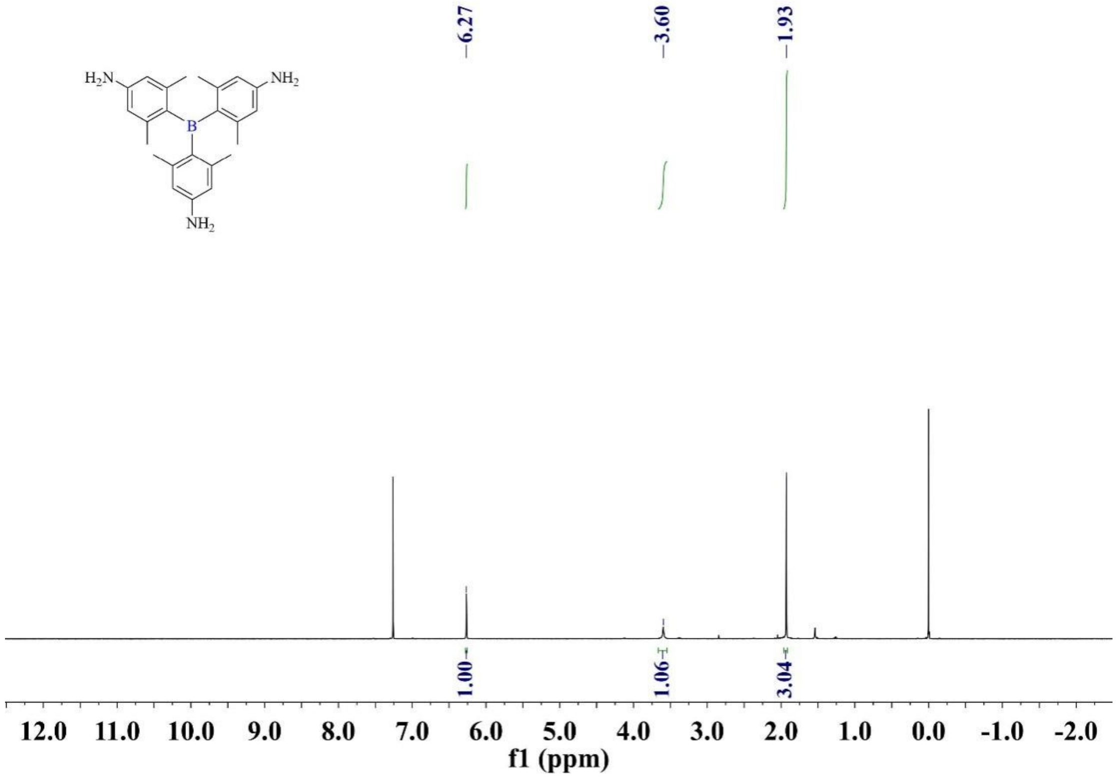

Figure S1. ^{1}H NMR of 4,4',4''-boranetriyltris(3,5-dimethylaniline) ($CDCl_3$).

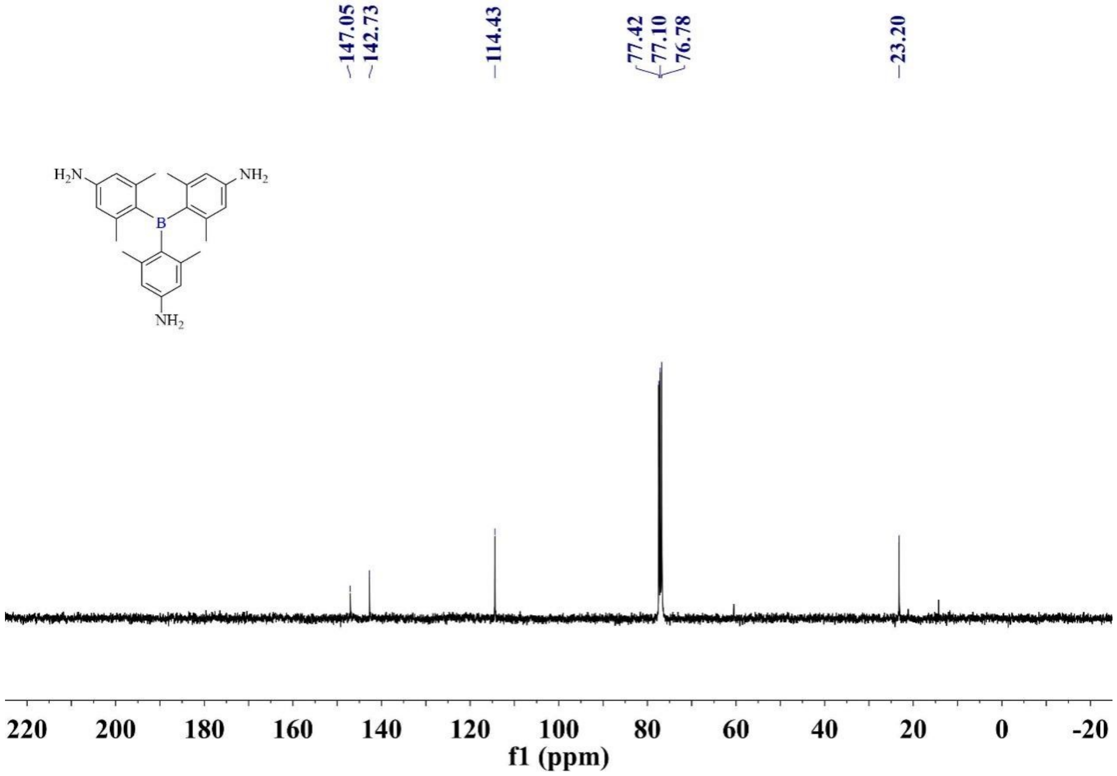

Figure S2. ^{13}C NMR of 4,4',4''-boranetriyltris(3,5-dimethylaniline) ($CDCl_3$).

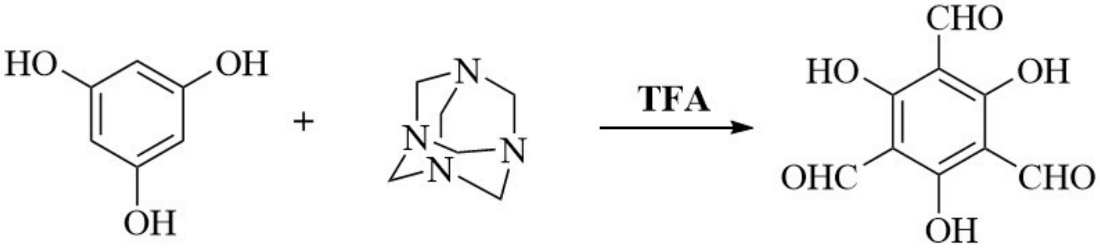

Scheme S2. Synthesis route of 2,4,6-triformylphloroglucinol (**TFP**).

3.2 Synthesis of 2,4,6-triformylphloroglucinol (**TFP**)[7]**:** In an argon atmosphere, phloroglucin (6.01 g, 49.0 mmol) and methenamine (15.1 g, 10.8 mmol) were dissolved in trifluoroacetic acid (TFA, 90 mL), the mixture were stirred and refluxed at 100 °C for 2.5 h. Then 100 mL HCl (aq., 3 M) was added and stirred for 1 h. After the reaction over, filtered, extracted with CH_2Cl_2 (100 mL × 3), washed with brine (50 mL), dried over $MgSO_4$, filtered, and the solvent was removed under reduced pressure to get a pink solid. The crude material was recrystallized from ethyl acetate to yield gray solid (1.48 g, 21.1 %). ^{1}H NMR (400 MHz, $CDCl_3$): δ 10.16 (s, 3H, Ar-C*H*O). ^{13}C NMR (100 MHz, $CDCl_3$): δ 192.04, 173.55, 102.85.

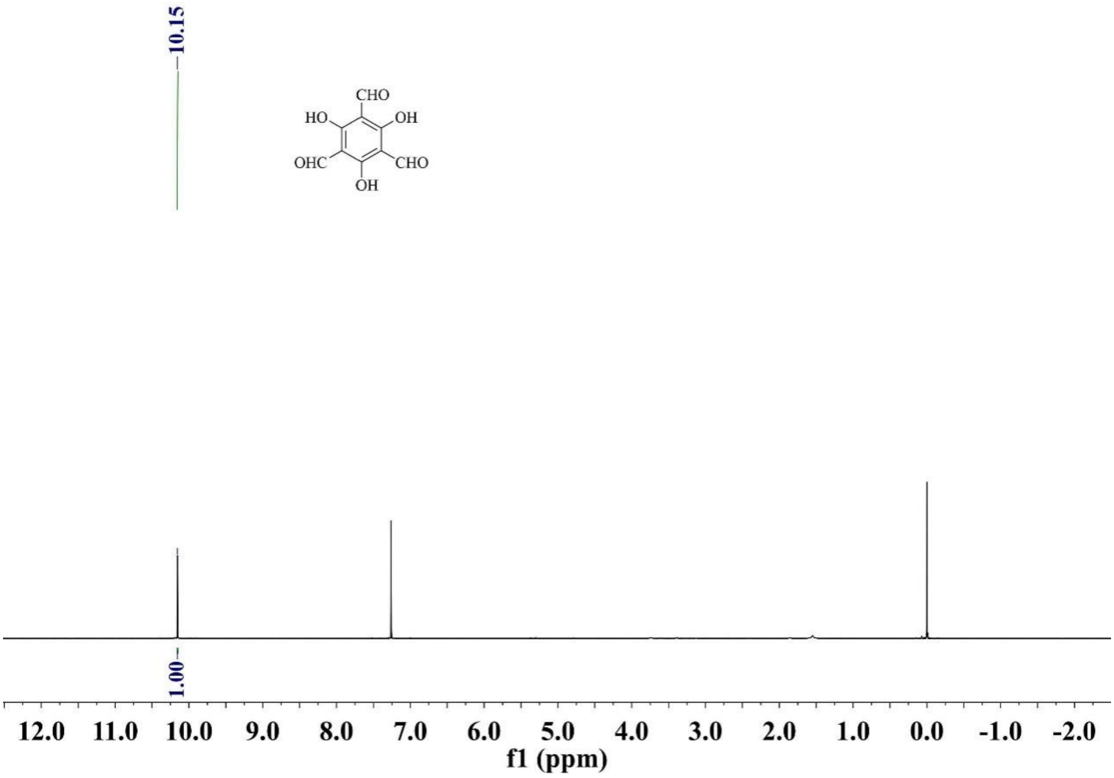

Figure S3. ^{1}H NMR of 2,4,6-triformylphloroglucinol ($CDCl_3$).

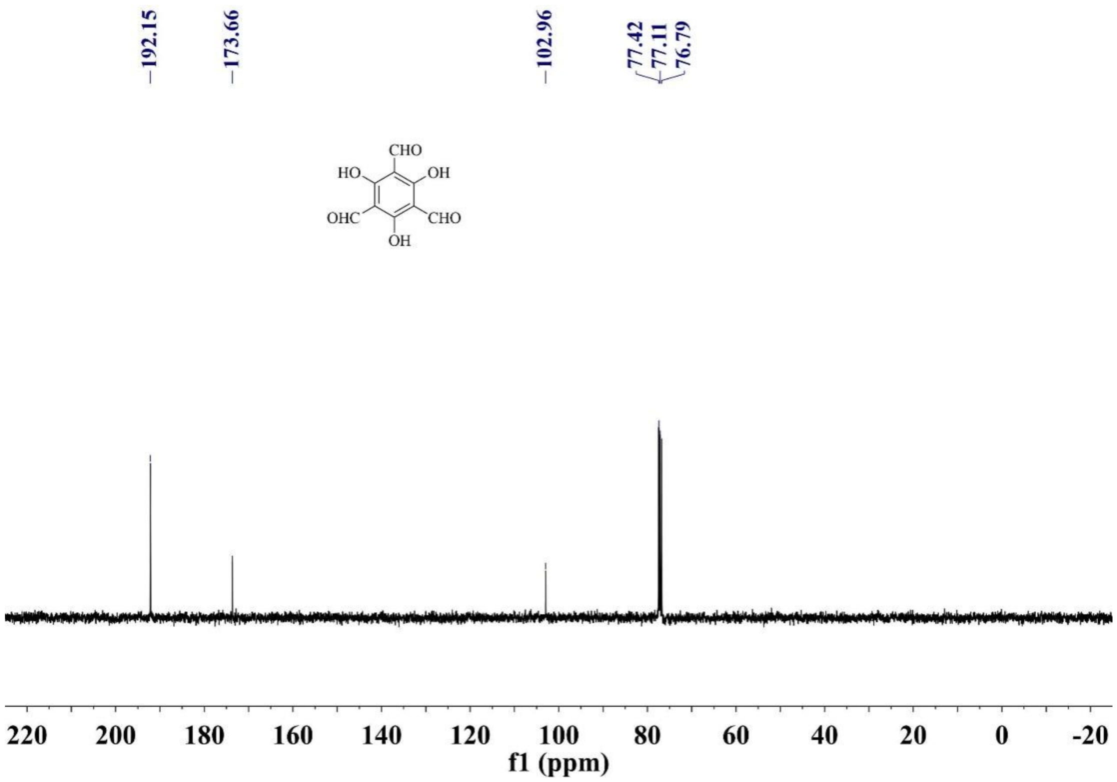

Figure S4. ^{13}C NMR of 2,4,6-triformylphloroglucinol ($CDCl_3$).

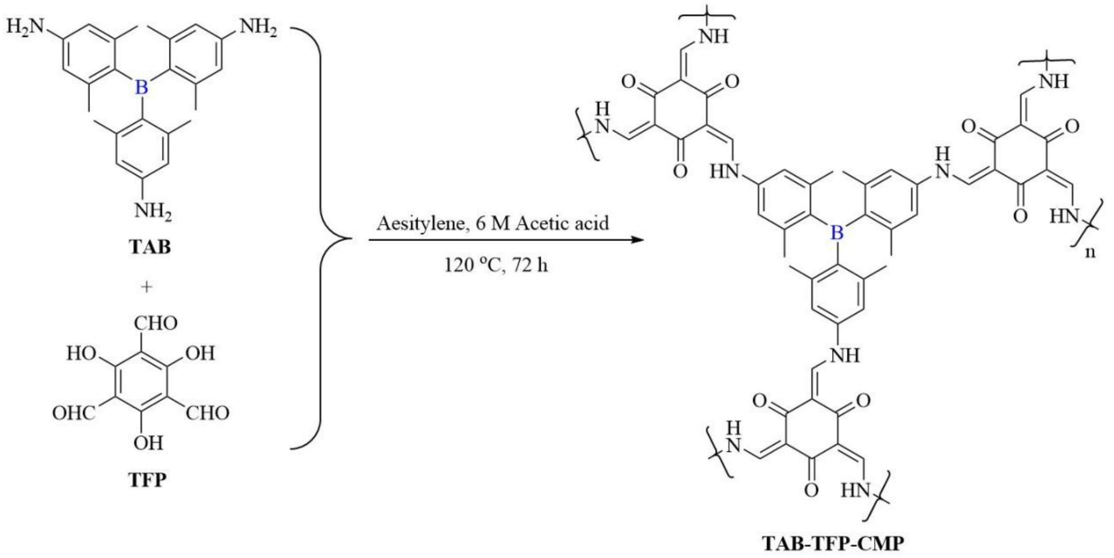

Scheme S3. Synthesis route of **TAB-TFP-CMP.**

3.3 Synthesis of TAB-TFP-CMP

To a 20 mL flask with Ar atmosphere, monomer **TAB** (148.5 mg, 0.40 mmol) and **TFP** (0.40 mmol, 84 mg) were suspended in the mixture solution of mesitylene (5 mL) and acetic acid (6 M, 0.5 mL) by ultrasonication at room temperature for 15 min. The mixture was then degassed through three freeze-pump-thaw cycles (vacuum < 50 mTorr) and heated at in an oven at 120°C for 72 h. After cooling to room temperature, a red brown powder was obtained by filtration. Then the solid was extracted through a Soxhlet extractor using THF as extracting solution for 48 h and dried at 60 °C for 24 h under vacuum. Yield: 183 mg (78.7 %).

3.4 Synthesis of TAB-TFB-COF

To a flame-dried 10 mL high-pressure flask with vacuum valve, **TAB** (29.7 mg, 0.08 mmol) and **TFB** (13.0 mg, 0.08 mmol) were suspended in a mixture 0.50 mL mesitylene, 0.50 mL dioxane and 0.1 mL 6 M acetic acid by ultrasonication at room temperature for 15 min. The mixture was degassed through three freeze-pump-thaw cycles (vacuum < 50 mTorr). Then the flask was sealed and heated in an oven at 120 °C for 3 days at autogenous pressure. As a result, the flask was opened and the suspension was filtered and washed with THF. The crude solid was further extracted through a Soxhlet extractor using THF as extracting solution for 48 h and dried at 60 °C for 2 days under vacuum. Yield: 35.6 mg (83.3 %).

3.5 Synthesis of TAB-TFP-COF

To a flame-dried 10 mL high-pressure flask with vacuum valve, **TAB-TFB-COF** (38.3 mg, 0.08 mmol) and **TFP** (16.8 mg, 0.08 mmol) were suspended in a mixture 0.50 mL mesitylene, 0.50 mL dioxane and 0.1 mL 6 M acetic acid by ultrasonication at room temperature for 15 min. The mixture was degassed through three freeze-pump-thaw cycles (vacuum < 50 mTorr). Then the flask was sealed and heated in an oven at 120 °C for 3 days at autogenous pressure. As a result, the flask was opened and the suspension was filtered and washed with THF. The crude solid was further extracted through a Soxhlet extractor using THF as extracting solution for 48 h and dried at 60 °C for 2 days under vacuum. Yield: 38.0 mg (90.0 %).

4. Characterization

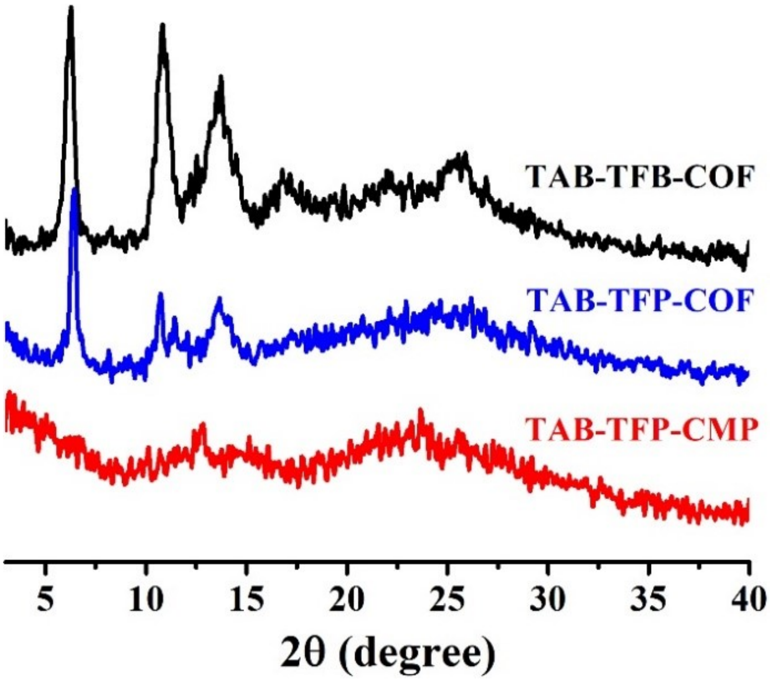

Figure S5. The PXRD patterns of **TAB-TFB-COF** (black), **TAB-TFP-COF** (blue) and **TAB-TFP-CMP** (red).

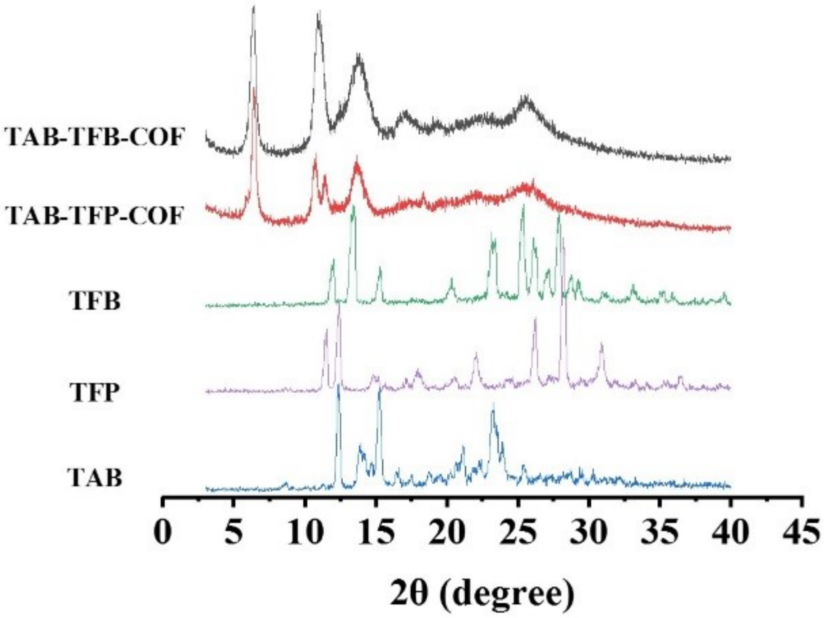

Figure S6. The PXRD patterns of precursors and sample COFs.

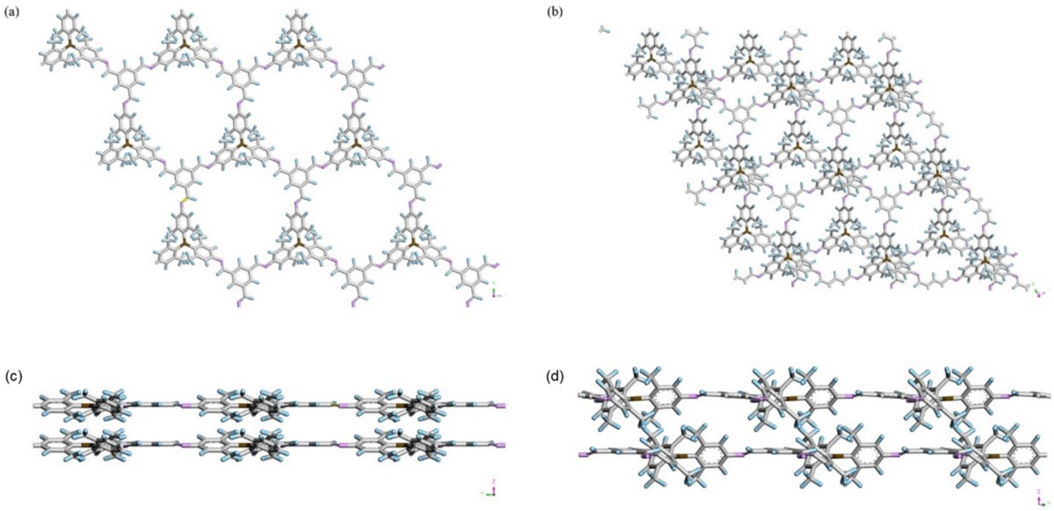

Figure S7. Simulated structure of **TAB-TFB-COF**. (a) Top and (b) side views of AA stacking model, (c) Top and (d) side views of AB stacking model.

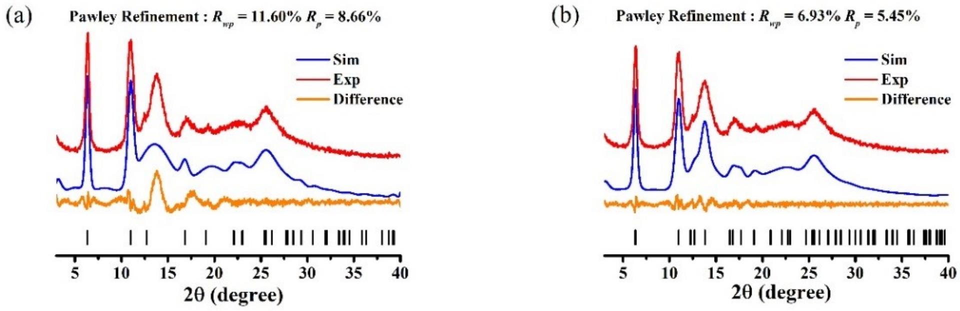

Figure S8. PXRD of **TAB-TFB-COF** with the corresponding Pawley refinement with different arrangement: (a) eclipsed, (b) staggered arrangement, and the difference curve (black line).

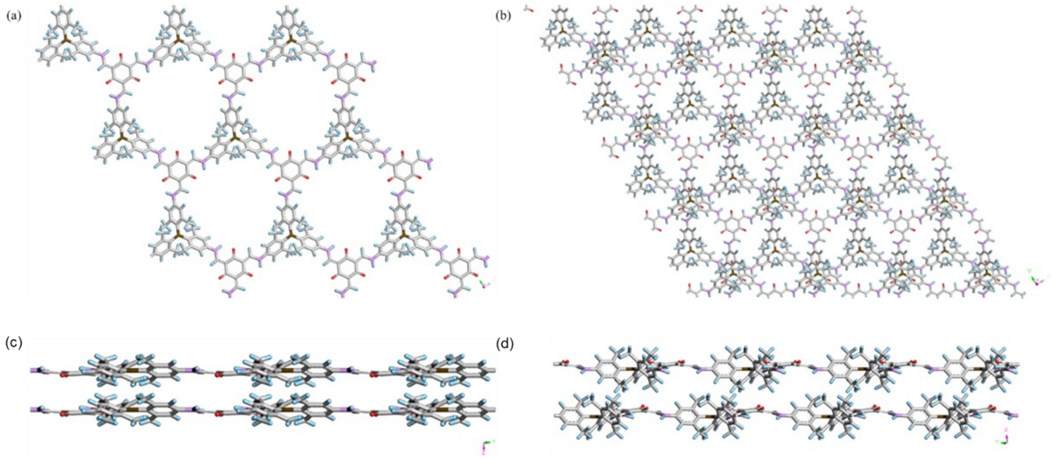

Figure S9. Simulated structure of **TAB-TFP-COF**. (a) Top and (b) side views of AA stacking model, (c) Top and (d) side views of AB stacking model.

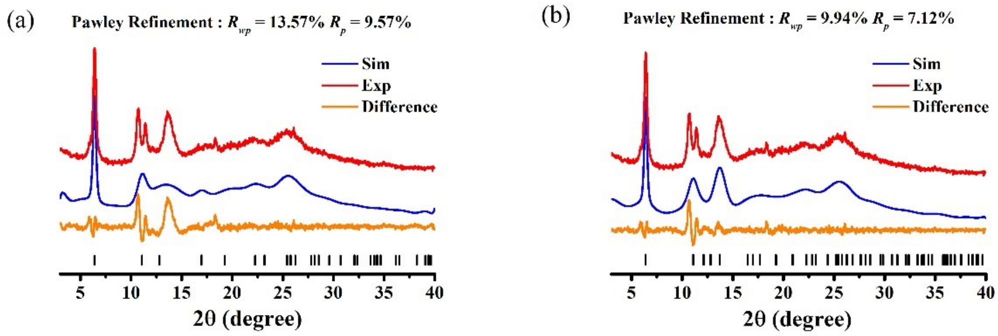

Figure S10. PXRD of **TAB-TFP-COF** with the corresponding Pawley refinement with different arrangement: (a) eclipsed, (b) staggered arrangement, and the difference curve (black) line). The R_{wp} and R_{p} values of **TAB-TFP-COF** are slightly higher, which may be related to the unidentified shoulder peak at around 11.6°.

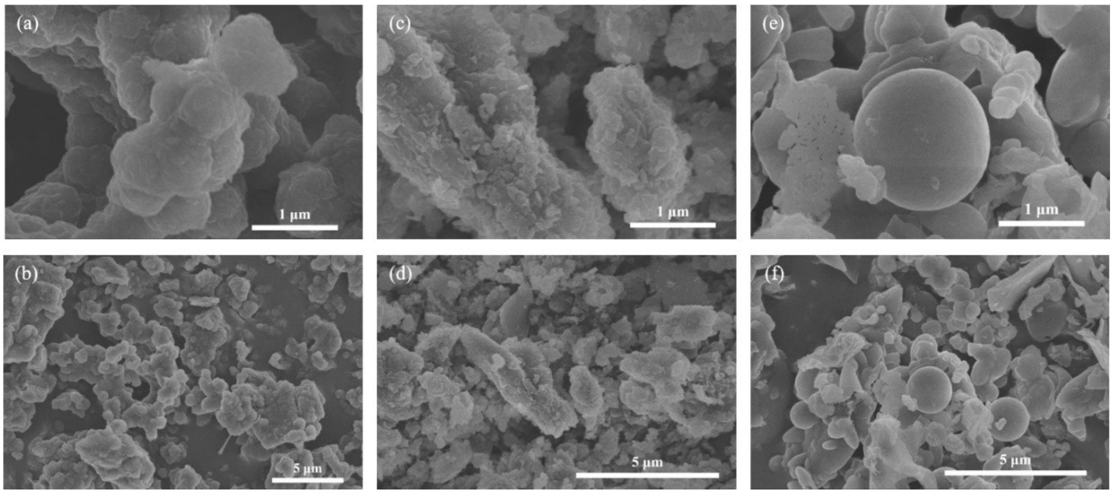

Figure S11. SEM images of (a) and (b) **TAB-TFB-COF**, (c) and (d) **TAB-TFP-COF**, and (e) and (f) **TAB-TFP-CMP**.

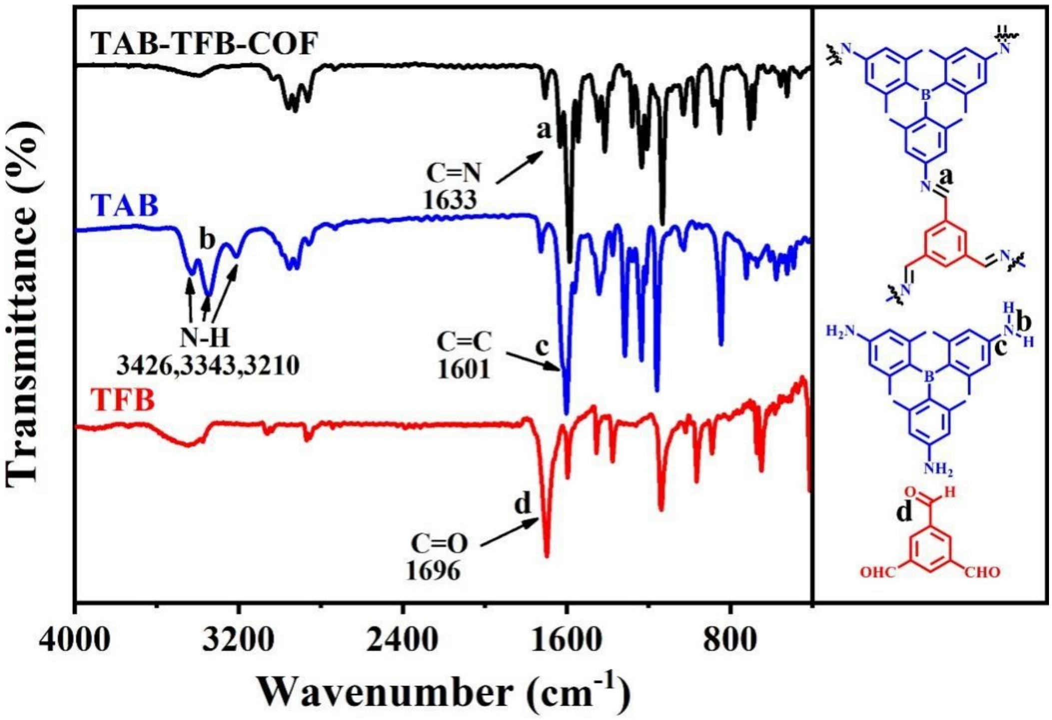

Figure S12. FT-IR spectra of **TAB** (blue), **TFB** (red) and **TAB-TFB-COF** (black).

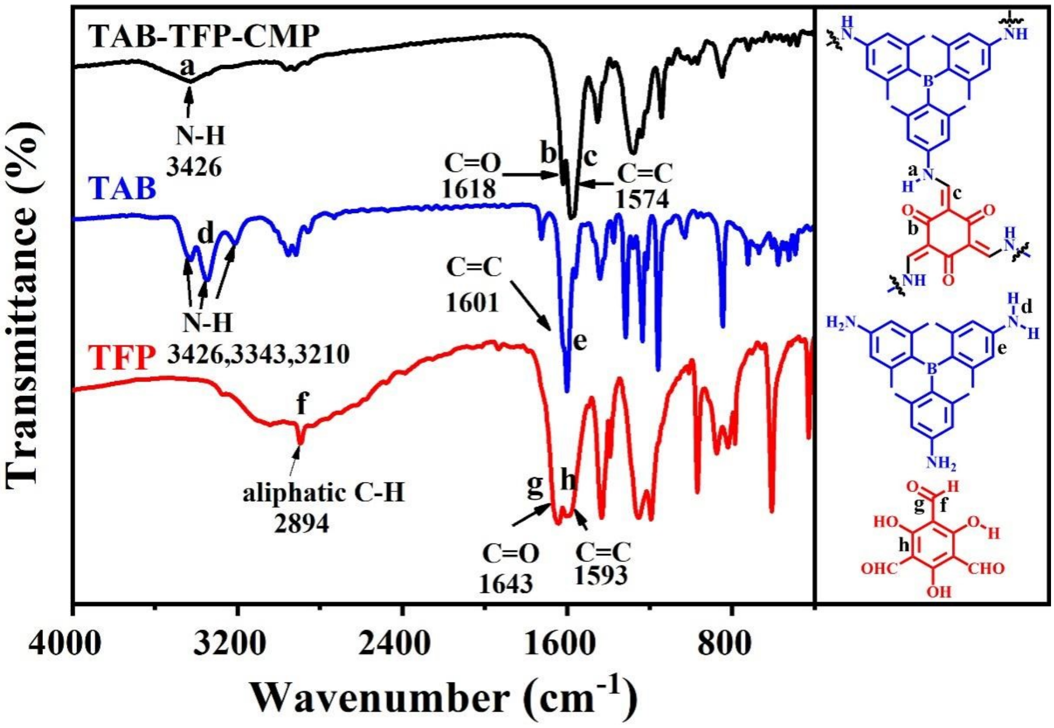

Figure S13. FT-IR spectra of **TAB** (blue), **TFP** (red) and **TAB-TFP-CMP** (black).

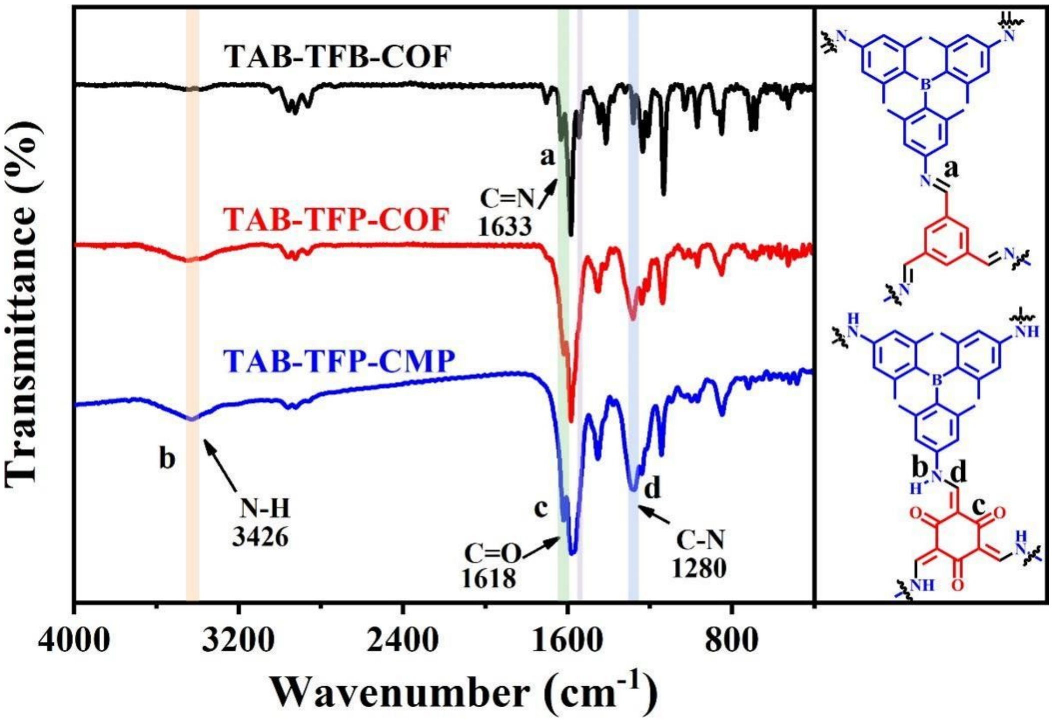

Figure S14. FT-IR spectra of **TAB-TFB-COF** (black), **TAB-TFP-COF** (red) and **TAB-TFP-CMP** (blue).

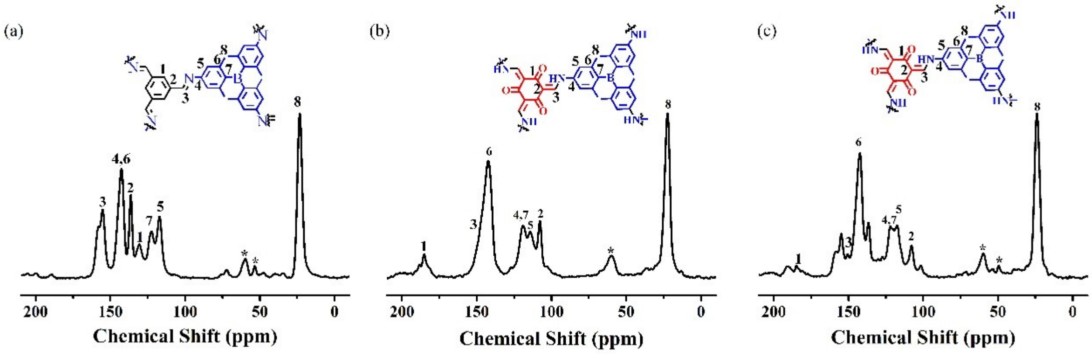

Figure S15. Solid ^{13}C CP-MAS NMR spectra of (a) **TAB-TFB-COF**, (b) **TAB-TFP-CMP**, and (c) **TAB-TFP-COF**.

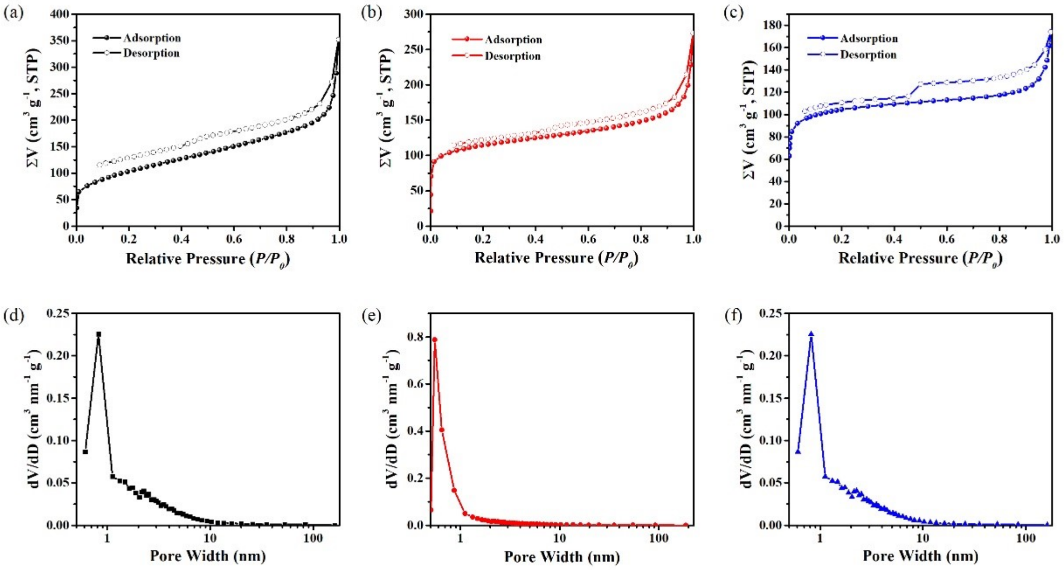

Figure S16. N_2 adsorption-desorption isotherms at 77 K of (a) **TAB-TFB-COF**, (b) **TAB-TFP-COF**, and (c) **TAB-TFP-CMP**. The pore size distribution curves for (d) **TAB-TFB-COF**, (e) **TAB-TFP-COF**, and (f) **TAB-TFP-CMP**.

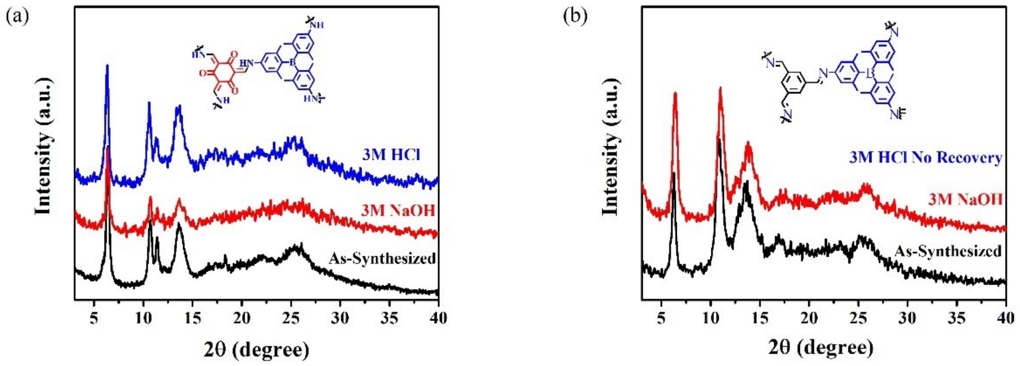

Figure S17. PXRD patterns of (a) **TAB-TFP-COF** and (b) **TAB-TFB-COF** before and after immersing in 3 M HCl and 3 M NaOH for 2 d.

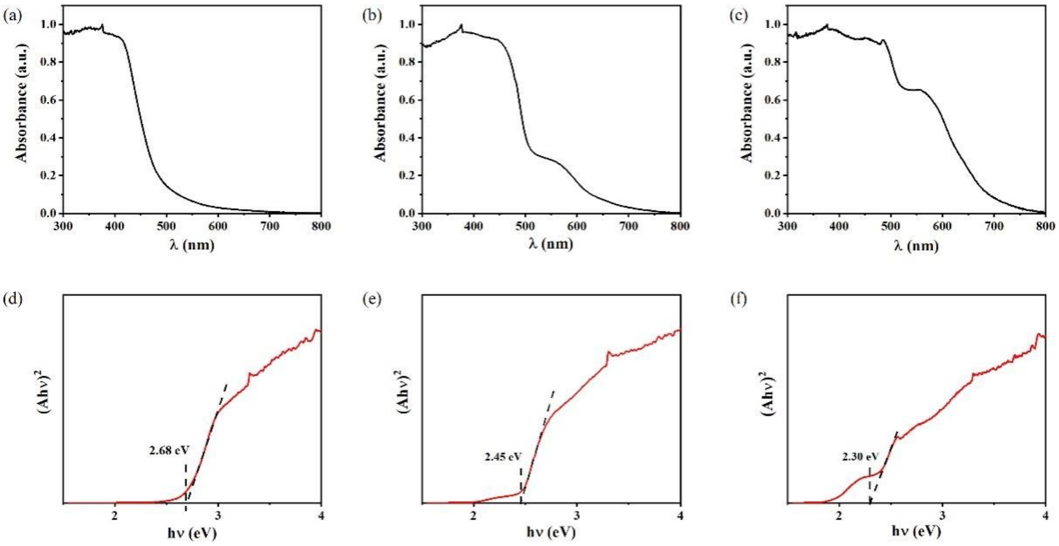

Figure S18. Solid UV-Vis absorption spectra of (a) **TAB-TFB-COF**, (b) **TAB-TFP-COF**, and (c) **TAB-TFP-CMP**. Kubelka−Munk function extracts the direct optical band gaps and the photographs of (d) **TAB-TFB-COF**, (e) **TAB-TFP-COF**, and (f) **TAB-TFP-CMP**.

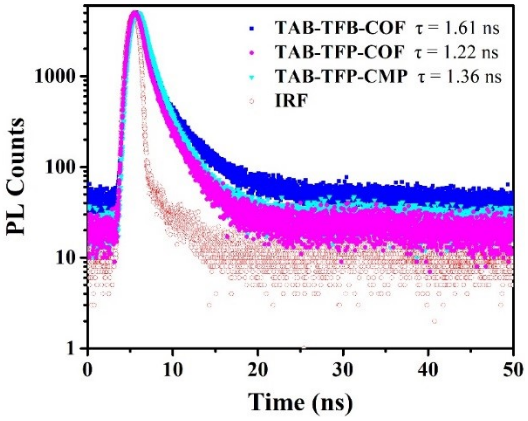

Figure S19. Photoluminescence lifetime spectra of **TAB-TFB-COF**, **TAB-TFP-COF** and **TAB-TFP-CMP**.

Table S1. The fitted photoluminescence lifetimes of powder samples

Sample	*λ_{ex} (nm)*	*λ_{em} (nm)*	*τ_1 (ns)*	*Rel.%*	*τ_2 (ns)*	*Rel.%*	*τ_3 (ns)*	*Rel.%*	*τ (ns)*
TAB-TFB-COF	360	558	0.43	40.91	1.45	36.60	4.00	22.49	1.61
TAB-TFP-COF	360	619	0.51	53.61	1.65	39.29	4.25	7.09	1.22
TAB-TFP-CMP	360	619	0.70	44.00	1.59	49.42	4.08	6.58	1.36
TAB-TFP-CMP-F	360	619	0.34	59.98	1.13	28.75	2.91	11.27	0.86

Table S2. Preliminary optimization of conditions for hydrogen production with **TAB-TFP-COF**

Entry	*Cat.（mg）*	*co-cat.* *(H_2PtCl_6)*	*Sol.* *(mL)*[a]		*SED*	*pH*[b]	*Amount of H_2 production* *(μmol h^{-1})*
1	10.0	3%	H_2O 20.0	——	TEOA 5 mL	——	0.342
2	10.0	3%	H_2O 20.0	——	TEA 5 mL	——	0.589
3	10.0	3%	H_2O 25.0	——	L-AA 0.1 M	——	4.510
4	10.0	3%	H_2O 20.0	——	MeOH 5 mL	——	0
5	10.0	3%	H_2O 25.0	——	AA+NaA 0.1 M	2.6 (2.7)[c]	4.510
6	10.0	3%	H_2O 25.0	——	AA+NaA 0.1 M	4.0 (4.2)[c]	4.241
7	10.0	3%	H_2O 25.0	——	AA+NaA 0.1 M	6.0 (6.3)[c]	0.873
8	10.0	3%	H_2O 25.0	——	AA+NaA 0.1 M	8.6 (7.2)[c]	0
9	10.0	3%	H_2O 25.0	MeOH 0.0	AA 0.1 M	——	4.510
10	10.0	3%	H_2O 20.0	MeOH 5.0	AA 0.1 M	——	7.486
11	10.0	3%	H_2O 15.0	MeOH 10.0	AA 0.1 M	——	5.516
12	10.0	3%	H_2O 10.0	MeOH 15.0	AA 0.1 M	——	2.924
13	10.0	3%	H_2O 5.0	MeOH 20.0	AA 0.1 M	——	0.73
14	10.0	3%	H_2O 0.0	MeOH 25.0	AA 0.1 M	——	0
15	10.0	3%	H_2O 20.0	MeOH 5.0	AA 0.1 M	——	7.486

16	10.0	3%	H_2O	EtOH	AA	——	5.350
			20.0	5.0	0.1 M		
17	10.0	3%	H_2O	MeCN	AA	——	2.769
			20.0	5.0	0.1 M		
18	10.0	3%	H_2O	THF	AA	——	0
			20.0	5.0	0.1 M		
19	10.0	3%	H_2O	MeOH	NA	——	0
			20.0	5.0			
20	10.0	3%	H_2O	MeOH	AA	——	5.767
			20.0	5.0	0.05 M		
21	10.0	3%	H_2O	MeOH	AA	——	7.486
			20.0	5.0	0.1 M		
22	10.0	3%	H_2O	MeOH	AA	——	7.267
			20.0	5.0	0.15 M		
23	10.0	3%	H_2O	MeOH	AA	——	3.692
			20.0	5.0	0.20 M		
24	10.0	0	H_2O	MeOH	AA	——	0
			20.0	5.0	0.1 M		
25	10.0	1.5%	H_2O	MeOH	AA	——	4.051
			20.0	5.0	0.1 M		
26	10.0	3%	H_2O	MeOH	AA	——	7.486
			20.0	5.0	0.1 M		
27	10.0	4.5%	H_2O	MeOH	AA	——	5.908
			20.0	5.0	0.1 M		
28	10.0	6%	H_2O	MeOH	AA	——	5.343
			20.0	5.0	0.1 M		
29	10.0	3%	H_2O	MeOH	AA	——	7.486
			20.0	5.0	0.1 M		
30[d]	10.0	3%	H_2O	MeOH	AA	——	0
			20.0	5.0	0.1 M		

a: The volume of the reaction solvent was 25ml.

b: pH was regulated by buffer system of L-ascorbic acid (HA) / L-sodium ascorbate (NaA). The pH of catalytic system was estimated according to the equation as follows: $pH = pK_a + log\frac{[A^-]}{[HA]}$

pKa of the L-ascorbic acid is 4.17.

Sacrificial agent: AA = Ascorbic Acid, NaA = Sodium Ascorbate, TEOA = Triethanolamine, TEA = Triethylamine.

c: pH values in parentheses are the average of three measurements by pH meter.

d: The reaction took place under dark conditions.

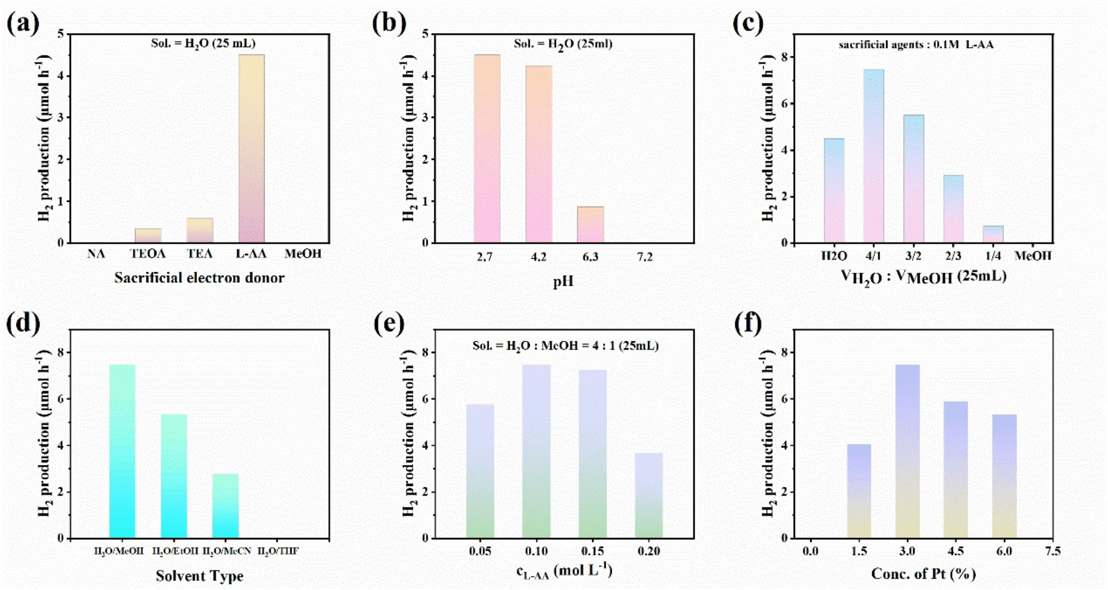

Figure S20. Conditions optimized of photocatalytic hydrogen production from water splitting reaction. (a) Different kinds of sacrificial agent, (b) different pH value, (c) different volume ratio (V_{H_2O}:V_{MeOH}) of the reaction solution, (d) different solvents, (e) different concentration of L-AA, and (f) different concentration of co-catalyst (Pt) for **TAB-TFP-COF** to hydrogen evolution rate.

Table S3. Dependence of H_2 production on photocatalyst concentration

Entry	*Cat[a] (mg)*	*Cat. Conc. (g L^{-1})*	*Amount of H_2 production[b] (μmol h^{-1})*			*Mean (μmol h^{-1})*	*Standard Deviation*	*HER Rate[c] (μmol h^{-1} g^{-1})*
31	0	0	0	0	0	0	0	0
32	2.5	0.1	2.581	2.466	2.373	2.473	0.10419	989.2
33	5	0.2	4.709	4.605	4.801	4.705	0.09806	941.0
34	7.5	0.3	5.765	5.836	5.747	5.783	0.04713	771.1
35	10	0.4	7.519	7.438	7.500	7.486	0.04236	748.6
36	12.5	0.5	8.358	8.298	8.347	8.334	0.03185	666.72
37	15	0.6	6.771	6.718	6.693	6.727	0.03991	448.5
38	20	0.8	5.209	5.401	5.499	5.370	0.14732	268.5
39	30	1.2	3.994	4.132	3.902	4.009	0.11561	133.6

a: Pretreatment of catalyst: Pt was loaded under light for 1h with the optimized conditions (Entry 29), and the catalyst was centrifuged, washed and dried with water and methanol for later use.

b. Three different batches of catalysts were used for the HER reaction.

c. The rate of hydrogen production calculated by per unit mass.

Table S4. Calculated AQY at different wavelength of **TAB-TFP-COF**

λ (nm)	*Amount of H_2 production[a] (μmol h^{-1})*		*Power (W m^{-2})*	*AQY (%)*
420	1.077	1.009	50.1	0.686
450	1.189	1.144	160	0.224
500	0.567	0.706	190	0.093
550	0.252	0.214	181	0.033
600	0.166	0.158	198	0.019

a. Two different batches of catalysts were used for the HER reaction.

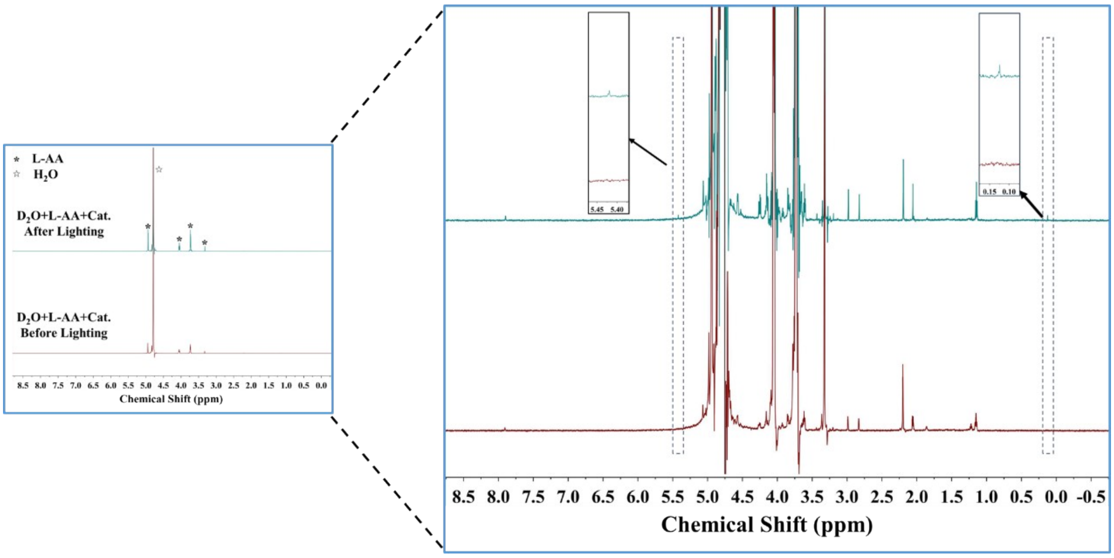

Figure S21. ^1H NMR spectra of system (D_2O+L-AA+Cat.) before and after 5 h illumination.

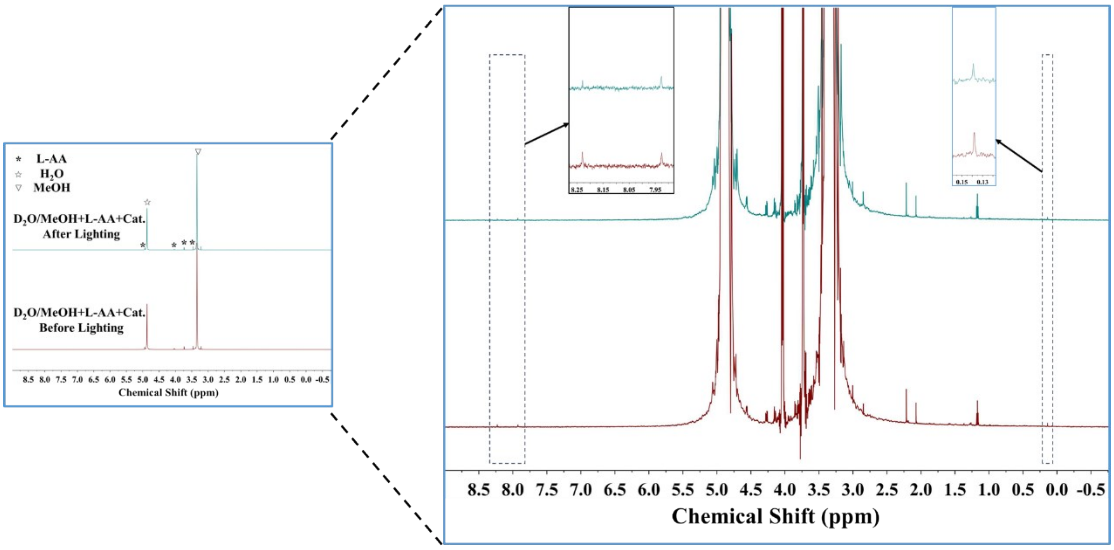

Figure S22. ^1H NMR spectra of system (D_2O/MeOH+L-AA+Cat.) before and after 5 h illumination.

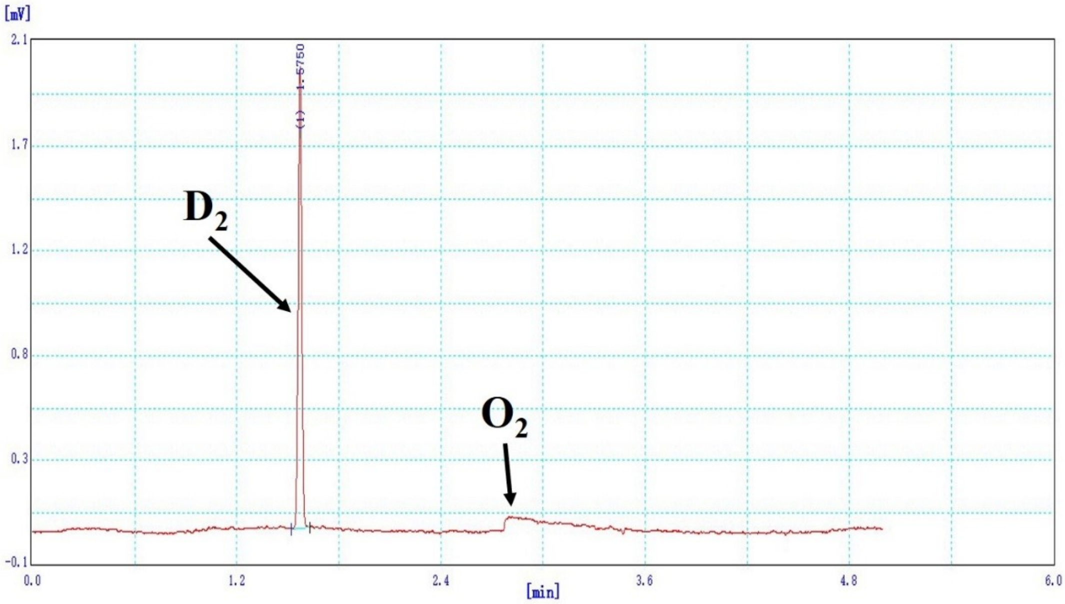

Figure S23. Gas chromatogram of system (D_2O/MeOH+L-AA+Cat.) after 5 h illumination.

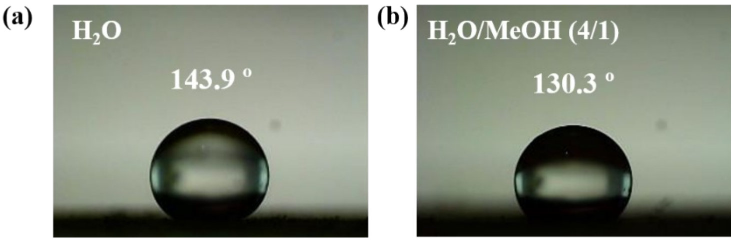

Figure S24. Contact angle of **TAB-TFP-COF** (a) H_2O and (b) H_2O/MeOH=4:1.

A photocatalytic system containing 20 ml of D_2O, 12.5 mg of Pt-loaded photocatalyst and 0.1 M L-ascorbic acid was prepared. Sampling 1 after ultrasonication and bubbling was carried out; then the reaction was carried out under light for 5 hours, and then sampling again was marked as 2. Subsequently, 5 ml of anhydrous methanol was added to the system, and after stirring, the sampling was marked as 3. Finally, the system continued to be illuminated for 5 hours and then sampled marked as 4. The changes in the reaction solution were monitored by ^{1}H NMR, and the gas components generated by the reaction was detected by gas chromatography.

From **Figure S21**, in the system (D_2O+L-AA+Cat.), two new signals appeared at 0.12 ppm and 5.42 ppm after illumination, proving the progress of the photocatalytic reaction in this system. From **Figure S22**, no new NMR signal was generated in the ^{1}H NMR spectrum after illumination, which proved that no new species such as HCHO or HCOOH were generated in the photocatalytic system (D_2O/MeOH+L-AA+Cat.). Besides, only D_2 and O_2 (introduced by manual injection) peaks were detected by gas chromatography (**Figure S23**), indicating no CO or CO_2 was produced in the reaction system. Additionally, the contact angle test results (**Figure S24**) show that TAB-TFP-COF has better wettability in H_2O/MeOH=4/1, which means that MeOH increases the interfacial contact between the photocatalyst and the reaction solution. In summary, MeOH was not oxidize in this photocatalytic system but increases the interfacial contact between the photocatalyst and the reaction solution.

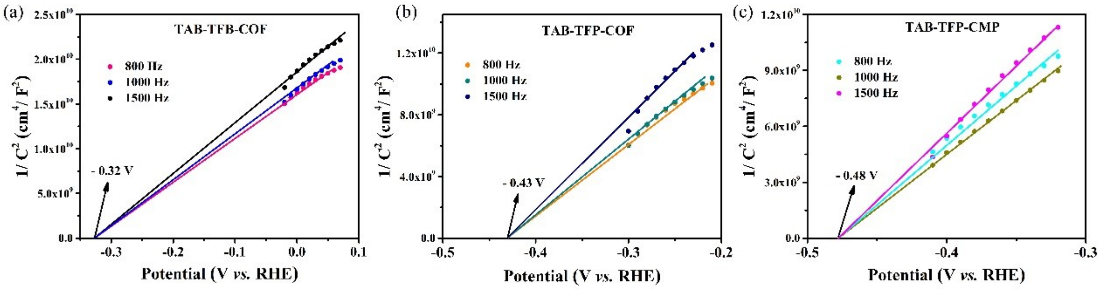

Figure S25. The Mott-Schottky plots of (a) **TAB-TFB-COF**, (b) **TAB-TFP-COF**, and (c) **TAB-TFP-CMP**.

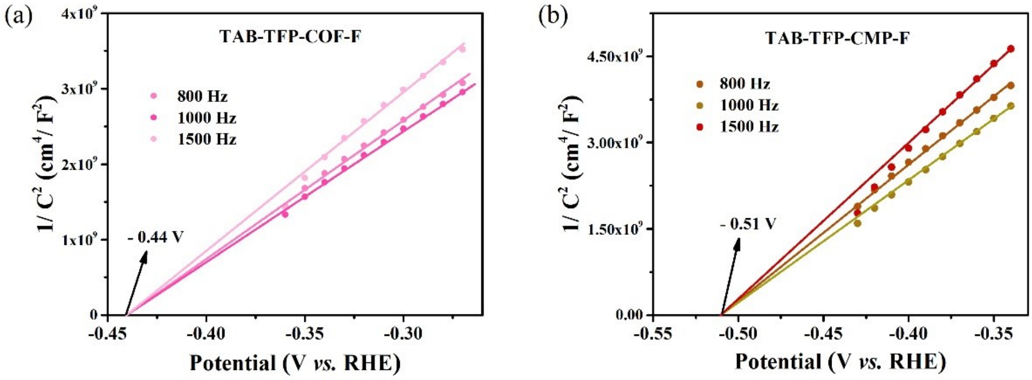

Figure S26. The Mott-Schottky plots of (a) **TAB-TFB-COF-F** and (b) **TAB-TFP-COF-F**.

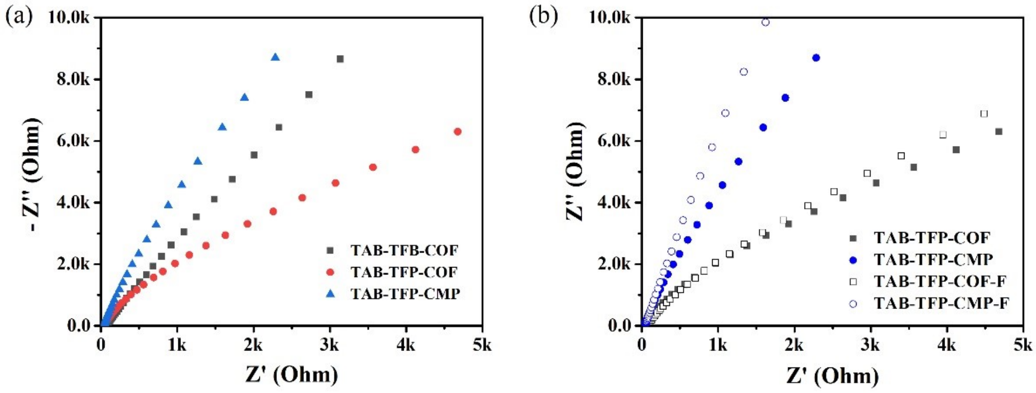

Figure S27. EIS Nyquist plots of (a) **TAB-TFB-COF**, **TAB-TFP-COF**, and **TAB-TFP-CMP**; and (b) **TAB-TFP-COF-F** and **TAB-TFP-CMP-F**.

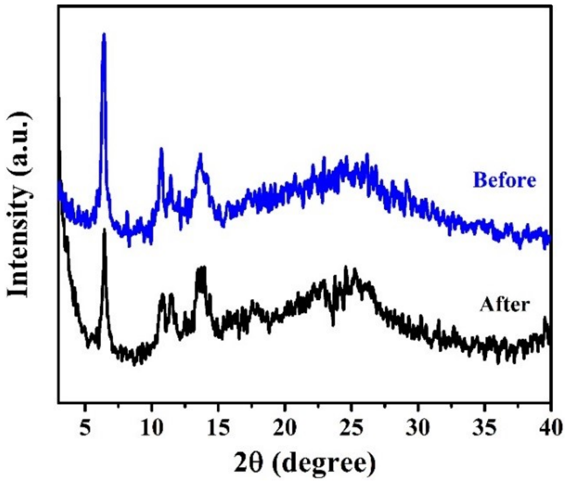

Figure S28. The PXRD of **TAB-TFP-COF** befor (red) and after (blue) 30 h irradiation with optimal condition for HER.

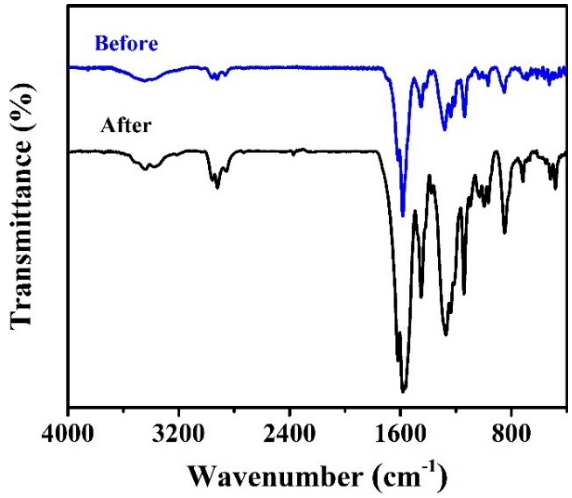

Figure S29. FT-IR spectra of **TAB-TFP-COF** befor (red) and after (blue) 30 h irradiation with optimal condition for HER.

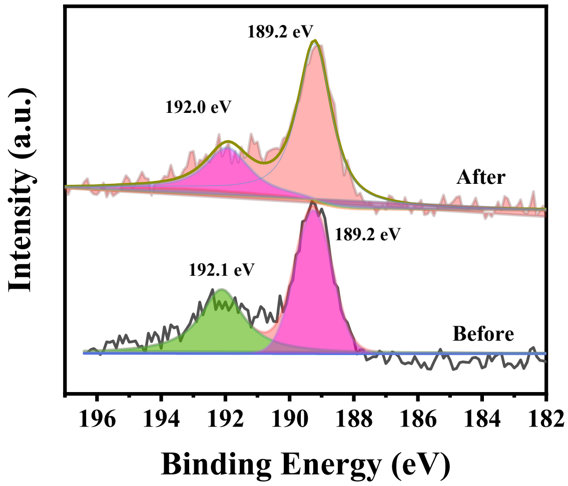

Figure S30. High-resolution XPS spectra of B 1s before and after 30 h irradiation with optimal condition for HER.

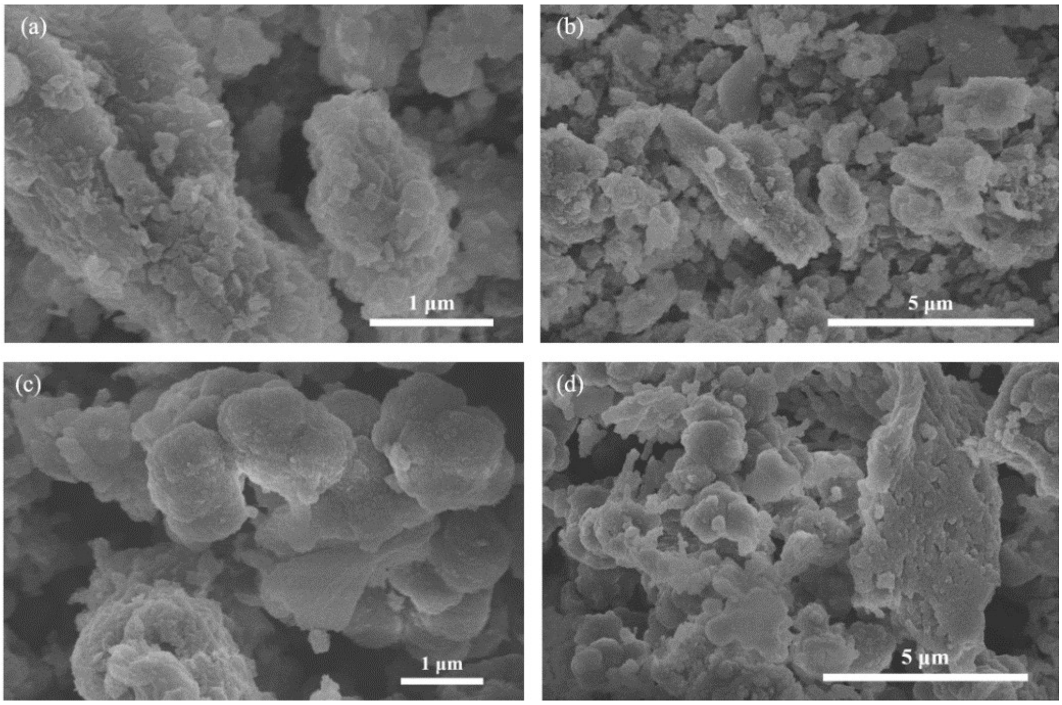

Figure S31. SEM images of **TAB-TFP-COF.** (a) and (b) before visible light irradiation**,** (c) and (d) after 30 h irradiation with optimal condition for HER.

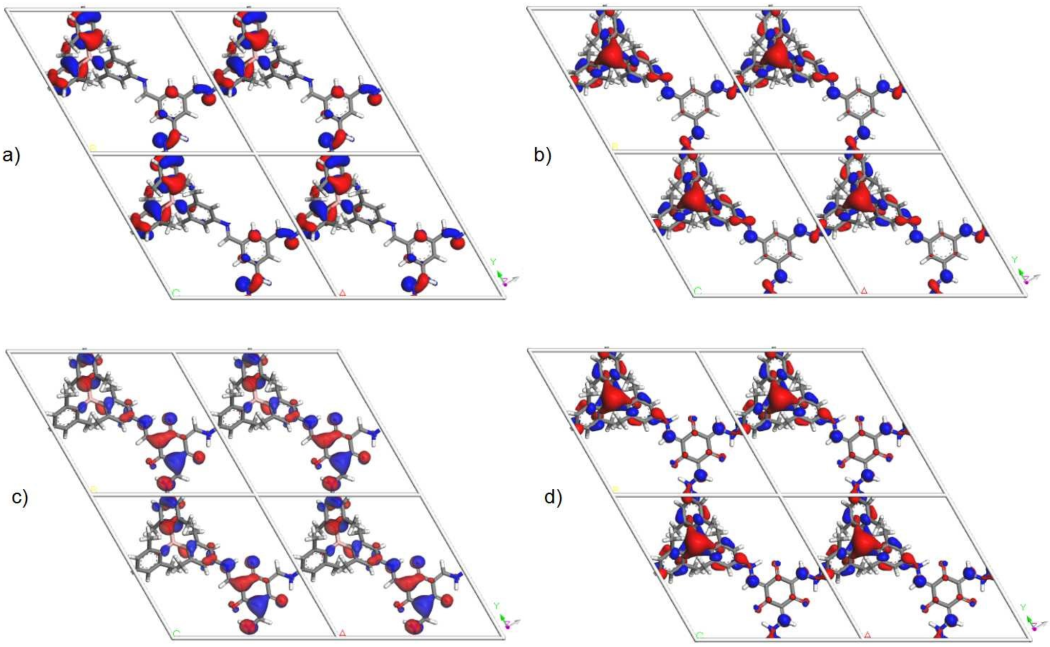

Figure S32. (**a**) HOMO and (b) LUMO orbitals distribution of **TAB-TFB-COF**, (c) HOMO and (d) LUMO orbitals distribution of **TAB-TFP-COF**.

Table S5. Photophysical properties and hydrogen production for photocatalysts.

Samples		**TAB-TFB-COF**	**TAB-TFP-COF**	**TAB-TFP-CMP**
E_{HOMO} (eV)[a]		1.29	1.14	-
E_{LUMO} (eV)[a]		-1.03	-0.65	-
E_g^{DFT} (eV)[a]		2.32	1.79	-
E_g^{opt} (eV)[b]		2.68	2.45	2.30
CB (eV)[c]		-0.32	-0.43	-0.48
BET (m^2 g^{-1})		358.1	353.4	323.1
H_2 production	Amount (μmol h^{-1})	0.11	8.34	6.12
	Rates per gram (μmol h^{-1} g^{-1})	8.8	666.4	489.6
	Surface area normalization (μmol h^{-1} m^{-2})	0.025	1.89	1.52

[a] DFT calculation results. [b] Calculated from the onset of the solid absorption spectra. [c] Calculated from the Mott-Schottky plots. [d] Hydrogen evolution rates based on average over 5 h irradiation.

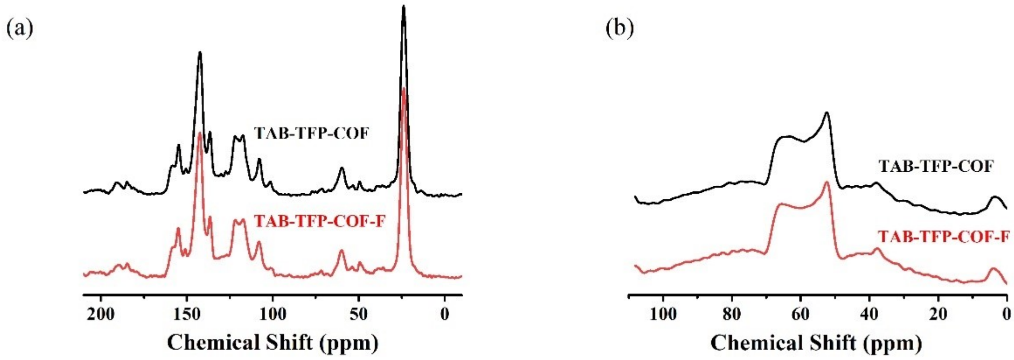

Figure S33. (a) Solid ^{13}C CP-MAS NMR spectra and (b) Solid ^{11}B sNMR spectra of **TAB-TFP-COF** (black) and **TAB-TFP-COF-F** (red).

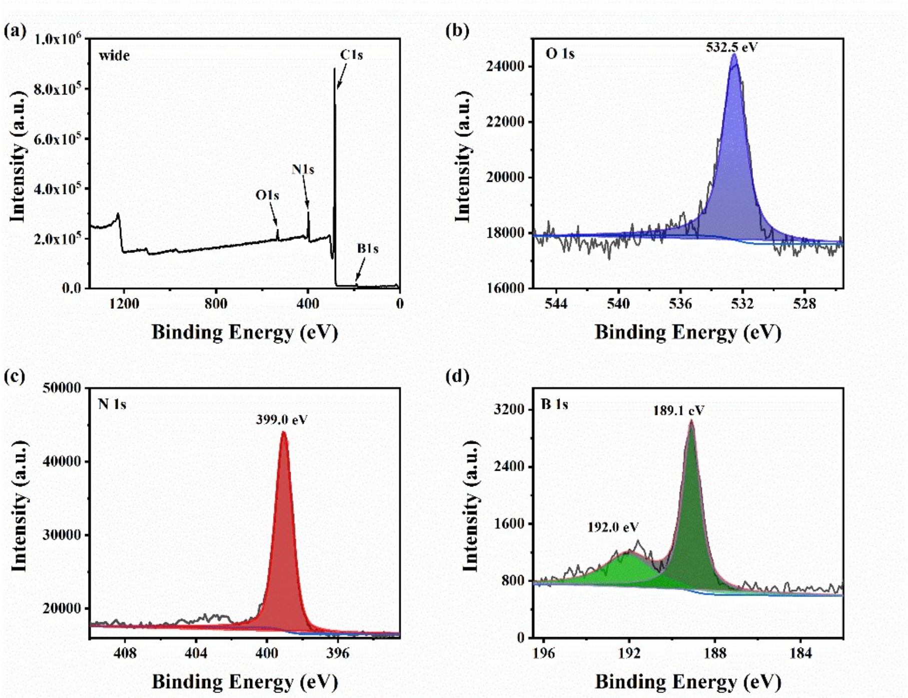

Figure S34. (a) XPS survey spectrum and high-resolution XPS spectra of (b) O 1s, (c) N 1s, and (d) B 1s of **TAB-TFB-COF**.

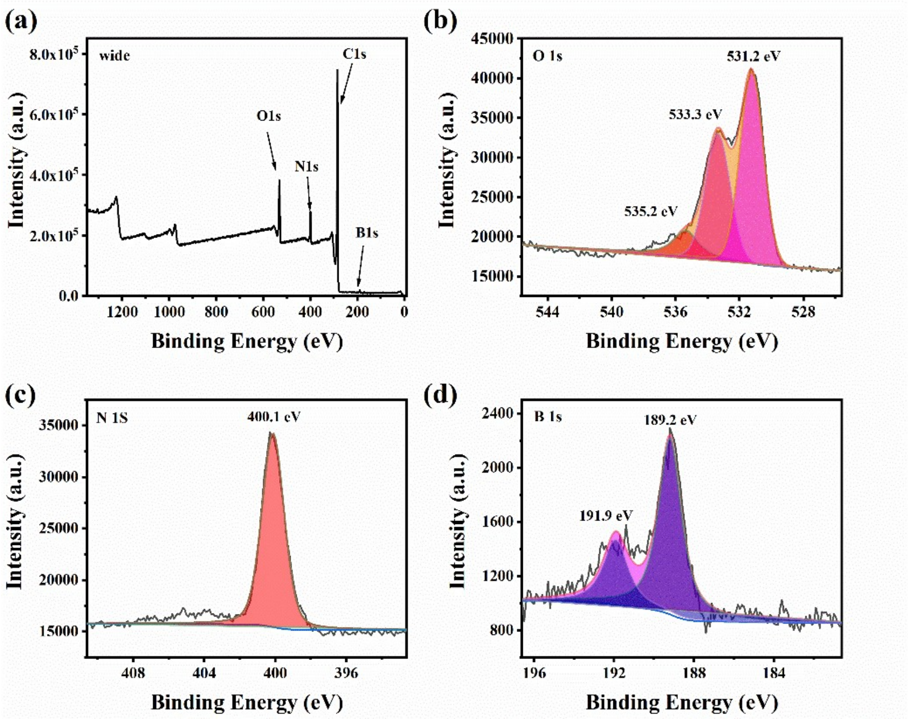

Figure S35. (a) XPS survey spectrum and high-resolution XPS spectra of (b) O 1s, (c) N 1s, and (d) B 1s of **TAB-TFP-CMP**.

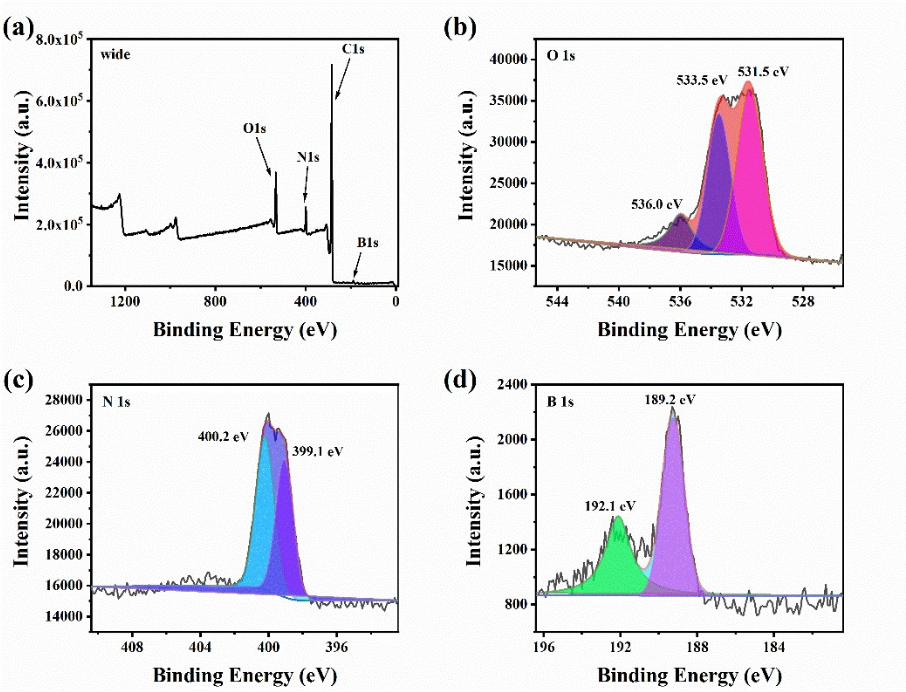

Figure S36. (a) XPS survey spectrum and high-resolution XPS spectra of (b) O 1s, (c) N 1s, (d) B 1s of **TAB-TFP-COF**.

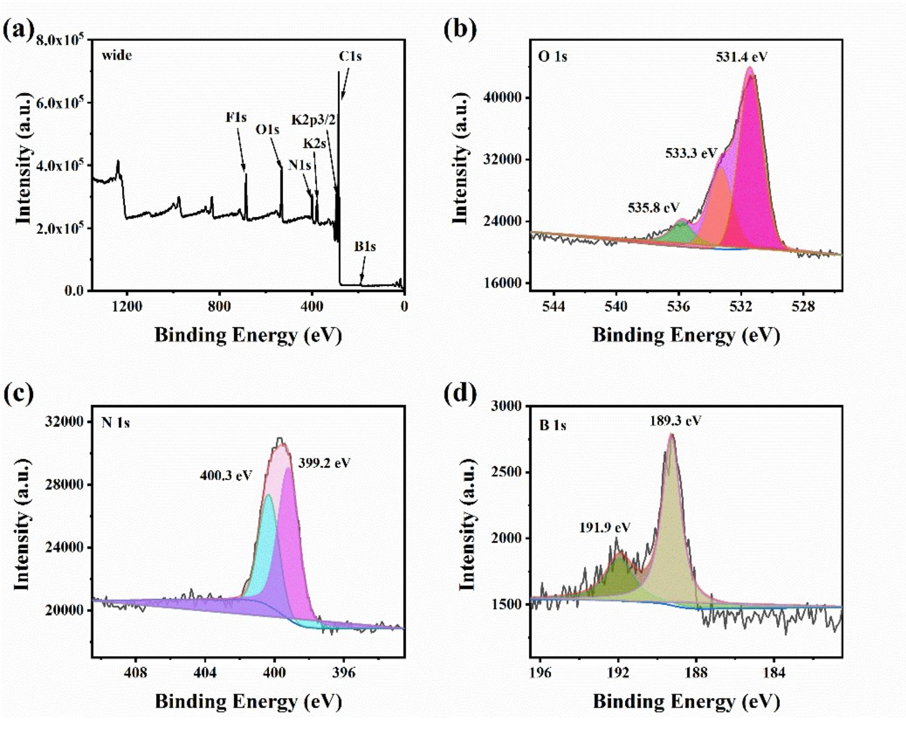

Figure S37. (a) XPS survey spectrum and high-resolution XPS spectra of (b) O 1s, (c) N 1s, (d) B 1s of **TAB-TFP-COF-F**.

Peak 1 at around 192 eV represents the signature of B in the **TAB**, while peak 2 at 189 eV corresponds to the B sub-oxide.[8]

Table S6. Atomistic coordinates for the AA-stacking mode of **TAB-TFB-COF** optimized using Dmol3 method (space group *P3*, $a = b = 16.094788$ Å, $c = 3.502347$ Å, $\alpha = \beta = 90°$ and $\gamma = 120°$).

Atom	***x / a***	***y / b***	***z / c***
C	0.46854	0.97548	0.69931
C	0.49753	0.93070	0.82311
C	0.45542	0.83294	0.82616
C	0.38189	0.77806	0.70138
C	0.35227	0.82444	0.57705
C	0.39558	0.92228	0.57988
N	0.56578	0.49051	0.69674
C	0.53793	0.40347	0.73400
C	0.60431	0.36818	0.73163
C	0.57009	0.27146	0.73179
C	0.48934	0.79014	0.96690
C	0.27644	0.77268	0.43756
H	0.55186	0.97225	0.92035
H	0.37354	0.95838	0.48678
H	0.46471	0.35463	0.76080
H	0.52842	0.75987	0.89989
H	0.42928	0.73479	1.04308
H	0.53696	0.84245	1.06788
H	0.29007	0.72279	0.36157
H	0.27274	0.82075	0.33630
H	0.20733	0.73424	0.50566
H	0.49531	0.22347	0.73246
B	0.33333	0.66667	0.70146

Table S7. Atomistic coordinates for the AB-stacking mode of **TAB-TFB-COF** optimized using Dmol3 method (space group *P3*, $a = b = 16.090838$ Å, $c = 7.21317$ Å, $\alpha = \beta = 90°$ and $\gamma = 120°$).

Atom	*x / a*	*y / b*	*z / c*
C	0.46839	0.97551	0.33369
C	0.49830	0.93071	0.41884
C	0.45637	0.83294	0.42055
C	0.38196	0.77807	0.33445
C	0.35139	0.82451	0.24899
C	0.39466	0.92237	0.25126
N	0.56601	0.49069	0.33221
C	0.53790	0.40343	0.35729
C	0.60429	0.36817	0.35599
C	0.57005	0.27143	0.35613
C	0.49173	0.79024	0.51712
C	0.27423	0.77287	0.15322
H	0.55329	0.97227	0.48606
H	0.37193	0.95856	0.18732
H	0.46449	0.35443	0.37488
H	0.52963	0.75922	0.46911
H	0.43277	0.73566	0.57324
H	0.54131	0.84295	0.58558
H	0.28698	0.72307	0.09805
H	0.26956	0.8212	0.08391
H	0.20569	0.73448	0.20208
H	0.49523	0.22343	0.35646
C	1.13555	0.30894	0.81560
C	1.16485	0.26403	0.90152
C	1.12247	0.16619	0.90370

C	1.04879	0.11144	0.81633
C	1.01919	0.15806	0.72953
C	1.06237	0.25593	0.73225
N	1.23222	-0.17653	0.81412
C	1.20427	-0.26370	0.83929
C	1.27080	-0.29875	0.83766
C	1.23679	-0.39540	0.83763
C	1.15641	0.12330	1.00232
C	0.94350	0.10664	0.63136
H	1.21963	0.30554	0.96904
H	1.04020	0.29229	0.66767
H	1.13096	-0.31274	0.85731
H	1.19379	0.09123	0.95529
H	1.09671	0.06954	1.05827
H	1.20605	0.17615	1.07086
H	0.95834	0.05863	0.57518
H	0.93831	0.15529	0.56301
H	0.87448	0.06633	0.67882
H	1.16199	-0.44357	0.83793
B	0.33333	0.66667	0.33437
B	1.00000	0.00000	0.81618

Table S8. Atomistic coordinates for the AA-stacking mode of **TAB-TFP-COF** optimized using Dmol3 method (space group *P3*, $a = b = 15.959733$ Å, $c = 3.503241$ Å, $\alpha = \beta = 90°$ and $\gamma = 120°$).

Atom	*x / a*	*y / b*	*z / c*
C	2.45310	-4.02660	0.46658
C	2.48499	-4.06824	0.59139
C	2.448250	-4.16517	0.59370
C	2.37632	-4.22270	0.46801
C	2.34324	-4.17968	0.34275
C	2.38204	-4.08247	0.34490
N	2.58210	-4.49045	0.46564
C	2.54985	-4.58721	0.50529
C	2.60694	-4.62278	0.53424
C	2.56458	-4.72533	0.55157
O	2.48130	-4.77212	0.58537
C	2.48640	-4.20431	0.73392
C	2.26807	-4.23448	0.20353
H	2.53785	-4.02465	0.68949
H	2.35756	-4.04931	0.24993
H	2.65054	-4.44703	0.41981
H	2.47491	-4.63545	0.50253
H	2.52887	-4.23024	0.66519
H	2.42839	-4.26252	0.80877
H	2.53165	-4.15128	0.83635
H	2.28419	-4.28292	0.12896
H	2.26138	-4.18872	0.10068
H	2.19964	-4.27516	0.27313
B	2.33333	-4.33333	0.46804

Table S9. Atomistic coordinates for the AB-stacking mode of **TAB-TFP-COF** optimized using Dmol3 method (space group *P3*, $a = b = 15.949081$ Å, $c = 7.297876$ Å, $\alpha = \beta = 90°$ and $\gamma = 120°$).

Atom	*x / a*	*y / b*	*z / c*
C	0.45434	0.97388	0.21417
C	0.48673	0.93173	0.29872
C	0.44948	0.83469	0.29979
C	0.37689	0.77755	0.21346
C	0.34348	0.82116	0.12839
C	0.38243	0.91843	0.13100
N	0.58111	0.50801	0.21431
C	0.54882	0.41148	0.24278
C	0.60632	0.37635	0.26116
C	0.56481	0.27407	0.27422
O	0.48241	0.22706	0.30224
C	0.48829	0.79516	0.39514
C	0.26734	0.76691	0.03311
H	0.54055	0.97496	0.36549
H	0.35721	0.95196	0.06713
H	0.64929	0.55086	0.18122
H	0.47384	0.36318	0.24243
H	0.53019	0.76930	0.34603
H	0.43076	0.73671	0.44728
H	0.53445	0.84802	0.4653
H	0.28316	0.71919	-0.02096
H	0.25898	0.81315	-0.03527
H	0.19961	0.72547	0.08241
C	0.78810	0.64037	0.74570
C	0.82050	0.59926	0.83203

C	0.78343	0.50227	0.83510
C	0.71002	0.44405	0.75074
C	0.67615	0.48649	0.66455
C	0.71603	0.58384	0.66340
N	0.91365	0.17401	0.74301
C	0.88180	0.07768	0.77243
C	0.93942	0.04289	0.79274
C	0.89792	-0.05957	0.80449
O	0.81450	-0.10728	0.82677
C	0.82312	0.46383	0.93055
C	0.59852	0.43113	0.57190
H	0.87432	0.64330	0.89841
H	0.69143	0.61649	0.59706
H	0.98091	0.21596	0.70665
H	0.80692	0.02927	0.77115
H	0.86343	0.43597	0.88203
H	0.76610	0.40719	0.98579
H	0.87139	0.51806	0.99765
H	0.60881	0.37685	0.52605
H	0.59631	0.47592	0.49530
H	0.53028	0.39716	0.62128
B	0.33333	0.66667	0.21271
B	0.66667	0.33333	0.75274

Table S10. Photocatalytic hydrogen evolution performances of the different COF-based photocatalysts and other B-containing photocatalysts.

Photocatalyst	*Co-catalysis*	*SED*	*solution*	*Illumination*	*HER rate* ($\mu mol\ g^{-1}\ h^{-1}$)	*AQY*	*Ref.*
TAB-TFP-COF	**3% Pt**	**L-AA**	**H_2O/MeOH**	**> 420 nm**	**666.4**	**0.69% (420 nm)**	**This work**
TaPa-1-COF	3% Pt	L-AA	PBS Buffer	> 420 nm	1223	-	[9]
TFPT-COF	3% Pt	TEOA	H_2O	> 420 nm	1970	1.6% (500 nm)	[10]
N_0-COF	3% Pt	TEOA	PBS Buffer	> 420 nm	23	0.001% (450 nm)	[11]
N_1-COF	3% Pt	TEOA	PBS Buffer	> 420 nm	90	0.077% (450 nm)	[11]
N_2-COF	3% Pt	TEOA	PBS Buffer	> 420 nm	438	0.19% (450 nm)	[11]
N_3-COF	3% Pt	TEOA	PBS Buffer	> 420 nm	1703	0.44% (450 nm)	[11]
N_2-COF	Co-1	TEOA	ACN/ H_2O	AM 1.5	782	0.16% (400 nm)	[12]
TP-DTP	3% Pt	TEOA	H_2O	≥ 395 nm	20	-	[13]
TP-EDDA	3% Pt	TEOA	H_2O	≥ 395 nm	30	-	[13]
TP-BDDA	3% Pt	TEOA	H_2O	> 395 nm	324	1.8% (520 nm)	[13]
AI-TCPP	0.1% Pt	TEOA	ACN/ H_2O	> 420 nm	50	-	[14]
PTP-COF	8% Pt	TEOA	PBS Buffer	AM 1.5	83.83	-	[15]
A-TEBPY-COF	3% Pt	TEOA	PBS Buffer	AM 1.5	98	-	[16]
A-TENPY-COF	3% Pt	TEOA	PBS Buffer	AM 1.5	22	-	[16]
A-TEPPY-COF	3% Pt	TEOA	PBS Buffer	AM 1.5	6	-	[16]
FS-COF	8% Pt	L-AA	H_2O	> 420 nm	10100	3.2% (420 nm)	[17]
S-COF	8% Pt	L-AA	H_2O	> 420 nm	4440	-	[17]
TP-COF	8% Pt	L-AA	H_2O	> 420 nm	1601	-	[17]
sp^2-COF	3% Pt	TEOA	H_2O	> 420 nm	1360	-	[18]
sp^2-COF$_{ERDN}$	3% Pt	TEOA	H_2O	> 420 nm	2120	0.48% (495 nm)	[18]
NTU-BDA-THTA	3% Pt	L-AA	AA/NaA Buffer	≥ 420 nm	1470	-	[19]
TaPa-1-COF	MoS2	L-AA	H2O	> 420 nm	5585	0.76% (420 nm)	[20]
Tapa-1-COF	3% Pt	L-AA	H2O	> 420 nm	5479	-	[20]

BtCOF-150	1% Pt	TEOA	H_2O	≥ 400 nm	750	0.2% (420 nm)	[21]
BtTpCOF	1% Pt	TEOA	H_2O	≥ 400 nm	450	-	[21]
BtAntCOF	1% Pt	TEOA	H_2O	≥ 400 nm	110	-	[21]
BT-COF	6% Pt	L-AA	H_2O	≥ 420 nm	76	-	[22]
TP-COF	6% Pt	L-AA	H_2O	≥ 420 nm	265	-	[22]
Tp-DTz-COF	8% Pt	TEOA	H_2O	≥ 420 nm	23	-	[23]
TaPa-COF-NO_2	3% Pt	L-AA	H_2O	≥ 420 nm	220	-	[24]
TaPa-COF	3% Pt	L-AA	H_2O	≥ 420 nm	1560	-	[24]
TaPa-COF-$(CH_3)_2$	3% Pt	L-AA	H_2O	≥ 420 nm	8330	-	[24]
Tp-PDA	3% Pt	NaA	H_2O	> 420 nm	600	-	[25]
Tp-DBN	3% Pt	NaA	H_2O	> 420 nm	1800	2.12% (420 nm)	[25]
TtaTfa_AC	8% Pt	L-AA	H_2O	> 420 nm	20700	1.43% (450 nm)	[26]
TpaTfa_AC	8% Pt	L-AA	H_2O	> 420 nm	14900	-	[26]
TtaTpa_AC	8% Pt	L-AA	H_2O	> 420 nm	10800	-	[26]
Py-CITP-BT	5% Pt	L-AA	H_2O	> 420 nm	8875	8.45 (420 nm)	[27]
Py-FTP-BT	5% Pt	L-AA	H_2O	> 420 nm	2875	-	[27]
Py-HTP-BT	5% Pt	L-AA	H_2O	> 420 nm	1078	-	[27]
BCN ceramic aerogels	1% Pt	TEOA	H_2O	> 420 nm	146	0.82 (420 nm)	[28]
BCN nanosheets	1% Pt	TEOA	H_2O	> 420 nm	112	0.54 (405 nm)	[29]
$B_{4.3}C$	2% Pt	MeOH	H_2O	> 420 nm	31	0.54 (420 nm)	[30]
BCN tubes	1% Pt	TEOA	H_2O	> 420 nm	56	0.32 (405 nm)	[31]
PB	1% Pt	HCHO	H_2O	> 420 nm	66	0.8 (420 nm)	[32]
BCN nanosheets	1% Pt	TEOA	H_2O	> 420 nm	82	-	[33]
Porous *h*-BN	-	TEOA	H_2O	-	47.1	-	[34]
PB2S	-	TEOA	H_2O	> 420 nm	223	0.0098% (420 nm)	[35]

References

(1) Abeles, F. *Optical properties of solids*; North-Holland Pub. Co., 1972.

(2) Davis, E. A.; Mott, N. F. Conduction in Non-Crystalline Systems V. Conductivity, Optical Absorption and Photoconductivity in Amorphous Semiconductors. *Philos. Mag.* **1970**, *22*, 0903-0922.

(3) Wu, K. F.; Du, Y. L.; Tang, H.; Chen, Z. Y.; Lian, T. Q. Efficient Extraction of Trapped Holes from Colloidal CdS Nanorods. *J. Am. Chem. Soc.* **2015**, *137*, 10224-10230.

(4) BIOVIA, D. S. BIOVIA Materials Studio, Version 8.0. 100.21. Dassault Systèmes, San Diego: 2014.

(5) Dilly, S.; Fotso, A. F.; Lejal, N.; Zedda, G.; Chebbo, M.; Rahman, F.; Companys, S.; Bertrand, H. C.; Vidic, J.; Noiray, M.; et al. From Naproxen Repurposing to Naproxen Analogues and Their Antiviral Activity against Influenza A Virus. *J. Med. Chem.* **2018**, *61*, 7202-7217.

(6) Yoshino, J.; Nakamura, Y.; Kunitomo, S.; Hayashi, N.; Higuchi, H. Synthesis of Tris(4-amino-2,6-dimethylphenyl)borane and Facile Extension of Its pi-Conjugated System by Utilizing the Reactivity of the Amino Groups. *Tetrahedron Lett.* **2013**, *54*, 2817-2820.

(7) Chong, J. H.; Sauer, M.; Patrick, B. O.; MacLachlan, M. J. Highly Stable Keto-Enamine Salicylideneanilines. *Org. Lett.* **2003**, *5*, 3823-3826.

(8) Ong, C. W.; Huang, H.; Zheng, B.; Kwok, R. W. M.; Hui, Y. Y.; Lau, W. M. X-Ray Photoemission Spectroscopy of Nonmetallic Materials: Electronic Structures of Boron and BxOy. *J. Appl. Phys.* **2004**, *95*, 3527-3534.

(9) Zhang, F. M.; Sheng, J. L.; Yang, Z. D.; Sun, X. J.; Tang, H. L.; Lu, M.; Dong, H.; Shen, F. C.; Liu, J.; Lan, Y. Q. Rational Design of MOF/COF Hybrid Materials for Photocatalytic H2 Evolution in the Presence of Sacrificial Electron Donors. *Angew. Chem., Int. Ed.* **2018**, *57*, 12106-12110.

(10) Stegbauer, L.; Schwinghammer, K.; Lotsch, B. V. A Hydrazone-Based Covalent Organic Framework for Photocatalytic Hydrogen Production. *Chem. Sci.* **2014**, *5*, 2789-2793.

(11) Vyas, V. S.; Haase, F.; Stegbauer, L.; Savasci, G.; Podjaski, F.; Ochsenfeld, C.; Lotsch, B. V. A Tunable Azine Covalent Organic Framework Platform for Visible Light-Induced Hydrogen Generation. *Nat. Commun.* **2015**, *6*, 8508.

(12) Banerjee, T.; Haase, F.; Savasci, G.; Gottschling, K.; Ochsenfeld, C.; Lotsch, B. V. Single-Site Photocatalytic H_2 Evolution from Covalent Organic Frameworks with Molecular Cobaloxime Co-Catalysts. *J. Am. Chem. Soc.* **2017**, *139*, 16228-16234.

(13) Pachfule, P.; Acharjya, A.; Roeser, J.; Langenhahn, T.; Schwarze, M.; Schomacker, R.; Thomas, A.; Schmidt, J. Diacetylene Functionalized Covalent Organic Framework (COF) for Photocatalytic Hydrogen Generation. *J. Am. Chem. Soc.* **2018**, *140*, 1423-1427.

(14) Fang, X. Z.; Shang, Q. C.; Wang, Y.; Jiao, L.; Yao, T.; Li, Y. F.; Zhang, Q.; Luo, Y.; Jiang, H. L. Single Pt Atoms Confined into a Metal-Organic Framework for Efficient Photocatalysis. *Adv. Mater.* **2018**, *30*, 1705112.

(15) Haase, F.; Banerjee, T.; Savasci, G.; Ochsenfeld, C.; Lotsch, B. V. Structure-Property-Activity Relationships in a Pyridine Containing Azine-Linked Covalent Organic Framework for Photocatalytic Hydrogen Evolution. *Faraday Discuss.* **2017**, *201*, 247-264.

(16) Stegbauer, L.; Zech, S.; Savasci, G.; Banerjee, T.; Podjaski, F.; Schwinghammer, K.; Ochsenfeld, C.; Lotsch, B. V. Tailor-Made Photoconductive Pyrene-Based Covalent Organic Frameworks for Visible-Light Driven Hydrogen Generation. *Adv. Energy Mater.* **2018**, *8*, 1703278.

(17) Wang, X. Y.; Chen, L. J.; Chong, S. Y.; Little, M. A.; Wu, Y. Z.; Zhu, W. H.; Clowes, R.; Yan, Y.; Zwijnenburg, M. A.; Sprick, R. S.; et al. Sulfone-Containing Covalent Organic Frameworks for

Photocatalytic Hydrogen Evolution from Water. *Nat. Chem.* **2018**, *10*, 1180-1189.

(18) Jin, E. Q.; Lan, Z. A.; Jiang, Q. H.; Geng, K. Y.; Li, G. S.; Wang, X. C.; Jiang, D. L. 2D sp(2) Carbon-Conjugated Covalent Organic Frameworks for Photocatalytic Hydrogen Production from Water. *Chem* **2019**, *5*, 1632-1647.

(19) Wang, H.; Qian, C.; Liu, J.; Zeng, Y. F.; Wang, D. D.; Zhou, W. Q.; Gu, L.; Wu, H. W.; Liu, G. F.; Zhao, Y. L. Integrating Suitable Linkage of Covalent Organic Frameworks into Covalently Bridged Inorganic/Organic Hybrids toward Efficient Photocatalysis. *J. Am. Chem. Soc.* **2020**, *142*, 4862-4871.

(20) Gao, M. Y.; Li, C. C.; Tang, H. L.; Sun, X. J.; Dong, H.; Zhang, F. M. Boosting Visible-Light-Driven Hydrogen Evolution of Covalent Organic Frameworks through Compositing with MoS2: A Promising Candidate for Noble-Metal-Free Photocatalysts. *J. Mater. Chem. A* **2019**, *7*, 20193-20200.

(21) Ghosh, S.; Nakada, A.; Springer, M. A.; Kawaguchi, T.; Suzuki, K.; Kaji, H.; Baburin, I.; Kuc, A.; Heine, T.; Suzuki, H.; et al. Identification of Prime Factors to Maximize the Photocatalytic Hydrogen Evolution of Covalent Organic Frameworks. *J. Am. Chem. Soc.* **2020**, *142*, 9752-9762.

(22) Ming, J. T.; Liu, A.; Zhao, J. W.; Zhang, P.; Huang, H. W.; Lin, H.; Xu, Z. T.; Zhang, X. M.; Wang, X. X.; Hofkens, J.; et al. Hot pi-Electron Tunneling of Metal-Insulator-COF Nanostructures for Efficient Hydrogen Production. *Angew. Chem., Int. Ed.* **2019**, *58*, 18290-18294.

(23) Biswal, B. P.; Vignolo-Gonzalez, H. A.; Banerjee, T.; Grunenberg, L.; Savasci, G.; Gottschling, K.; Nuss, J.; Ochsenfeld, C.; Lotsc, B. V. Sustained Solar H_2 Evolution from a Thiazolo 5,4-d thiazole-Bridged Covalent Organic Framework and Nickel-Thiolate Cluster in Water. *J. Am. Chem. Soc.* **2019**, *141*, 11082-11092.

(24) Sheng, J. L.; Dong, H.; Meng, X. B.; Tang, H. L.; Yao, Y. H.; Liu, D. Q.; Bai, L. L.; Zhang, F. M.; Wei, J. Z.; Sun, X. J. Effect of Different Functional Groups on Photocatalytic Hydrogen Evolution in Covalent-Organic Frameworks. *Chemcatchem* **2019**, *11*, 2313-2319.

(25) Wang, L. T.; Zhang, L. L.; Lin, B. Z.; Zheng, Y. Z.; Chen, J. L.; Zheng, Y.; Gao, B. F.; Long, J. L.; Chen, Y. L. Activation of Carbonyl Oxygen Sites in beta-Ketoenamine-Linked Covalent Organic Frameworks via Cyano Conjugation for Efficient Photocatalytic Hydrogen Evolution. *Small* **2021**, *17*, 2101017.

(26) Yang, J.; Acharjya, A.; Ye, M. Y.; Rabeah, J.; Li, S.; Kochovski, Z.; Youk, S.; Roeser, J.; Gruneberg, J.; Penschke, C.; et al. Protonated Imine-Linked Covalent Organic Frameworks for Photocatalytic Hydrogen Evolution. *Angew. Chem., Int. Ed.* **2021**, *60*, 19797-19803.

(27) Chen, W. B.; Wang, L.; Mo, D. Z.; He, F.; Wen, Z. L.; Wu, X. J.; Xu, H. X.; Chen, L. Modulating Benzothiadiazole-Based Covalent Organic Frameworks via Halogenation for Enhanced Photocatalytic Water Splitting. *Angew. Chem., Int. Ed.* **2020**, *59*, 16902-16909.

(28) Luo, Z. S.; Fang, Y. X.; Zhou, M.; Wang, X. C. A Borocarbonitride Ceramic Aerogel for Photoredox Catalysis. *Angew. Chem., Int. Ed.* **2019**, *58*, 6033-6037.

(29) Huang, C. J.; Chen, C.; Zhang, M. W.; Lin, L. H.; Ye, X. X.; Lin, S.; Antonietti, M.; Wang, X. C. Carbon-Doped BN Nanosheets for Metal-Free Photoredox Catalysis. *Nat. Commun.* **2015**, *6*, 7698.

(30) Liu, J. K.; Wen, S. H.; Hou, Y.; Zuo, F.; Beran, G. J. O.; Feng, P. Y. Boron Carbides as Efficient, Metal-Free, Visible-Light-Responsive Photocatalysts. *Angew. Chem., Int. Ed.* **2013**, *52*, 3241-3245.

(31) Chen, L. Y.; Wang, X. C. Bio-Templated Fabrication of Metal-Free Boron Carbonitride Tubes for Visible Light Photocatalysis. *Chem. Commun.* **2017**, *53*, 11988-11991.

(32) Shi, L.; Li, P.; Zhou, W.; Wang, T.; Chang, K.; Zhang, H. B.; Kako, T.; Liu, G. G.; Ye, J. H. n-Type Boron Phosphide as a Highly Stable, Metal-Free, Visible-Light Active Photocatalyst for Hydrogen Evolution. *Nano Energy* **2016**, *28*, 158-163.

(33) Chen, L. Y.; Zhou, M.; Luo, Z. S.; Wakeel, M.; Asiri, A. M.; Wang, X. C. Template-Free Synthesis of Carbon-Doped Boron Nitride Nanosheets for Enhanced Photocatalytic Hydrogen Evolution. *Appl. Catal., B* **2019**, *241*, 246-255.

(34) Liu, Q. W.; Chen, C.; Du, M.; Wu, Y. W.; Ren, C. J.; Ding, K. N.; Song, M. X.; Huang, C. J. Porous Hexagonal Boron Nitride Sheets: Effect of Hydroxyl and Secondary Amino Groups on Photocatalytic Hydrogen Evolution. *ACS Appl. Nano Mater.* **2018**, *1*, 4566-4575.

(35) Ru, C. L.; Wei, Q. Y.; Chen, W. H.; Guan, Q. Y.; Zhang, Q. Q.; Ling, Y.; Tao, C. L.; Qin, D. D.; Wu, J. C.; Pan, X. B. Tunable Conjugated Organoborane Oligomers for Visible-Light-Driven Hydrogen Evolution. *ACS Energy Lett.* **2020**, *5*, 669-675.